Intracranial Pressure Sensor

by

Xuan Zhang

A thesis submitted in partial fulfillment of

the requirements for the degree of

Master of Science

(Electrical and Computer Engineering)

At the

University of Wisconsin-Madison

Spring 2014

Contents

Background and motivation:

Hydrocephalus, also known as "water on the brain", is a medical condition in which there is excessive accumulation of cerebrospinal fluid (CSF) in the brain causing abnormal increase of Intracranial Pressure (ICP). Although Hydrocephalus occurs in every stage of life, it is more common with infants. It affects 1 in every 500 live births, making it one of the most common birth defects, more common than Down syndrome or deafness. The NIH website estimates 700,000 children and adults living with hydrocephalus, and it is by far the leading cause of brain surgery for children in the US. There are over 180 different causes of the condition, one of the most common being brain hemorrhage associated with premature birth. The US healthcare costs for hydrocephalus have exceeded $1 billion per year according to the Hydrocephalus Association [1], but it is still much less funded than research on other diseases, including juvenile diabetes, which has an incidence of about 0.2% in US children and adolescents in 2007

This kind of abnormal CSF accumulation can cause headaches, mental disability and death. Once the disease is identified, the fluid can be let out using the most commonly performed treatment for hydrocephalus the cerebral shunt to relieve the ICP. The shunt must be implanted into the patient's brain, a procedure which itself may cause brain damage. It is tunneled from the brain through the body and most commonly is inserted into a body cavity like the peritoneum (abdomen), pleura (chest), or heart. However, the cerebral shunt has changed very little since it was developed in 1906 and there is no known permanent cure for the disease and the CSF fluid will accumulate again. And another concern is the fact that detection of shunt failure is difficult. Therefore, early (timely) detection of elevated ICP is essential in reducing the risk of permanent brain damage and is very important to mitigate the Hydrocephalus symptoms during the entire life of the patient.

Physiology and Pathophysiology of Intracranial Pressure

Intracranial pressure (ICP) is the pressure inside the skull that fills in around the brain and spinal four brain ventricles as shown in Figure (1A). Its value, conventionally referenced to the atmospheric pressure

and expressed in millimeters of mercury, is maintained in a range between 7 and 15 mmHg for adults, 3–6 mmHg in children, and 1.5–6 mmHg in term infants [2]. The ICP value is essentially determined and significantly influenced by volume equilibrium among the brain (1,100−1,300 cm^3), CSF (130−150 cm^3) and blood contained in intracranial vessels (60−80 cm^3). Since the brain volume is fixed, the two most important determined factors of ICP are the cerebral blood flow, which is normally tightly regulated and remains nearly constant for a wide range of the mean arterial blood pressures [3], and the balance between the production of CSF in the choroid plexus of the brain ventricles and its absorption into the Dural venous sinuses.

Increased ICP is synonymous with volume expansion in the intracranial compartment. The volume expansion can be caused by a variety of reasons including intracranial hemorrhages, brain tumors, localized or generalized brain swelling and obstruction to CSF flow or absorption as shown in Table 1. A sigmoidal curve describes the exact relationship between intracranial volume changes and ICP as shown in Figure (1B). Volume expansion of up to 30 cm^3 usually results in insignificant changes of ICP because it can be compensated by extrusion of CSF from the intracranial cavity into the reservoir of the spinal theca, and, to a lesser extent, extrusion of venous blood from the cranium (region I in Figure (1B)). When the compensatory mechanisms have been exhausted, ICP rises rapidly with further increases in volume (region II in Figure (1B)) until it reaches the level comparable with the pressure inside of cerebral arterioles (which depends on mean arterial blood pressure and cerebrovascular resistance but normally measures between 50 and 60 mmHg). At this point the rise of ICP is halted as cerebral arterioles begin to collapse and the blood flow completely ceases (region III - the terminal plateau of the curve in Figure (1B). [4]

Table 1. Causes of Intracranial Hypertension (Grouped by Mechanism) [4]

Intracranial Causes	Extra-Cranial Causes
Intracranial masses	**Conditions leading to generalized brain swelling**
• Infarction (stroke) with edema	• Hypoxia (e.g. acute mountain sickness)
• Traumatic injuries with edema	• Hypertensive encephalopathy
• Hemorrhages (spontaneous or traumatic)	• Acute liver failure
• Brain tumors	• End-stage kidney failure
• Brain abscesses	• Hypercarbia (e.g. chronic pulmonary disease)
CSF accumulation	**Increased intracranial venous pressure**
• Increased CSF production (e.g. tumors of the choroid plexus)	• Cavernous sinus thrombosis
• Obstruction to CSF flow (non-communicating hydrocephalus)	• Obstruction of jugular veins • Superior vena cava syndrome
• Impaired CSF resorption (communicating hydrocephalus)	• Right heart failure

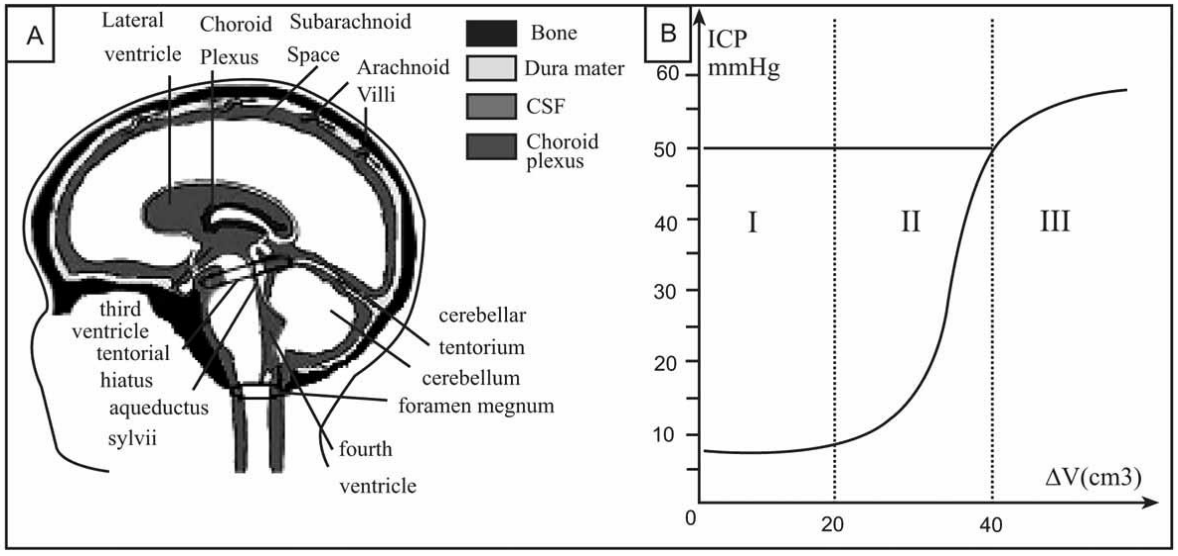

Figure 1 (**A**). Anatomy of the intracranial compartment; **(B)**. Intracranial pressure-volume curve (based on unpublished data from piglets). [4]

Role of ICP monitoring in current clinical practice

ICP is rarely monitored in patients comparing with other conditions accompanied with intracranial hypertension, including stroke. The main reason of this is that, operation of the risk together with complications and cost of treatment is significantly greater than guidance provided and clinical outcome and uncertain improvement in functional benefits. Therefore, most clinicians including neurosurgeons

prefer to rely on a combination of brain imaging such as CT or MRI and clinical observations including the subjective evaluation of symptoms and signs suggestive of IH such as headaches, confusion, papilledema or worsening neurological deficits. Exceptions are patients with hydrocephalus disease who have been implanted with a permanent catheter (shunt) that drains CSF into limited to patients in whom an intracranial catheter is primarily a therapeutic tool, such as patients with hydrocephalus who have been implanted with a permanent catheter (shunt) that drains abnormal accumulated CSF from the brain ventricular into the abdominal cavity. The more CSF accumulated without being drained in time, the more dangerous for the hydrocephalus patients. Therefore, timely detection of elevated ICP is essential in reducing the risk of permanent brain damage and is very important to mitigate the Hydrocephalus symptoms during the entire life of the patient.

Complications of intracranial pressure monitoring

Ventriculostomy catheter placement is the most common complication of infection with 5-14% incidence [5]. A study found there is no significant reduction/difference in infection rate for patients with prophylactic monitor changing before the fifth day with those whose catheters were placed for more than five days [6]. Use of antibiotic-coated ventriculostomy catheters is a feasible method to reduce the risk of infection from 9.4% to 1.3% [7]. Complications such as hemorrhage have an incidence of 1.4% and others such as malfunction, obstruction, and malposition occur.

Invasive Methods of Measuring ICP

The invasive method is the standard way for direct monitoring of ICP value. The standard technique is an invasive procedure that involves inserting a catheter into the intracranial compartment, usually through a small hole and connecting it to a standard pressure transducer [8]. Several different invasive methods of measuring ICP exist.

Catheter-Tip transducer

Catheter-tip transducers have been used for several years to record ICP. Miniature implantable transducers have been developed from intravascular transducers, of which the Camino transducer is an example as shown in Figure 2. Pressure is measured at the tip of a narrow fiber optic catheter where there is a flexible diaphragm. Light is reflected off the diaphragm and these changes in light intensity are interpreted in terms of pressure. The outside diameter of the device is only 1.3 mm. The system is not dependent on an external transducer.

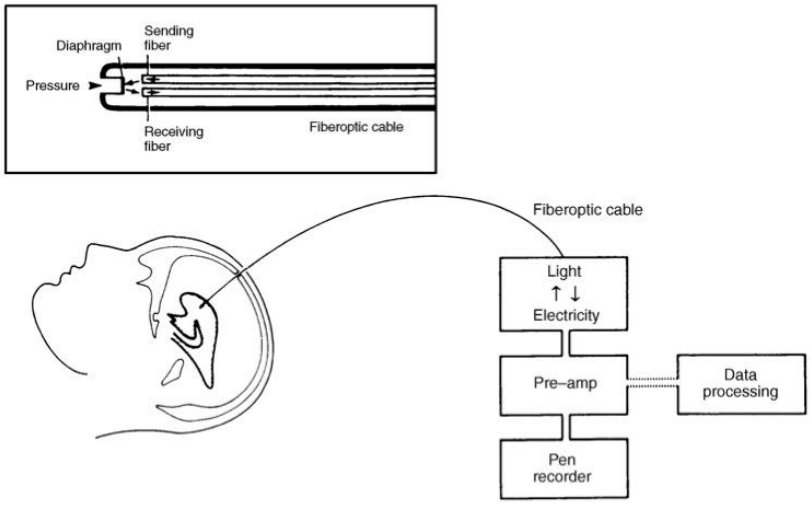

Figure 2 A catheter-tip transducer.

From Peter Reilly and Ross Bullock, *HEAD INJURY Pathophysiology and management of severe closed injury*, Fig. 10.4, P.212

Implanted microchip transducer

Implanted microchip sensors have now been developed and an example is the Codman Micro Sensor transducer. It consists of a miniature solid state pressure sensor as shown in Figure 3 mounted in a very small titanium case (diameter 1.2 mm) at the tip of a 100 cm long flexible nylon tube (diameter 0.7 mm). The transducer tip contains a silicon microchip with diffused piezoresistive strain gauges which are connected by wires in the nylon tube to complete a Wheatstone bridge type circuit. When the transducer is energized and pressure is applied, the silicon diaphragm deflects a small amount (less than 0.001 mm for 100 mmHg applied pressure), inducing strain in the embedded piezoresistors. This

resistance change is reflected in the form of a different voltage then converted into different pressure, i.e. mmHg. The bottom diaphragm layer is vented to the atmosphere along the nylon tube, while the top layer is exposed to the applied CSF or brain tissue pressure [4]. This technology represents the direction of ICP monitoring.

Transcutaneous pressure sensors currently used mostly after a shunt surgery cannot be permanently left in place, as they create a conduit for infection. The Codman ICP monitor, an example of a current system is shown in Figure 4. The Codman ICP pressure sensor uses a strain gauge to measure pressure – changes in pressure are registered as changes in the sensor resistance.

For a more long term use, the Codman ICP sensor must be fully encased within the patient, contain its own power source and be able to communicate wirelessly with a reader. A few attempts have been made to date to create such a system, most commonly using inductive coupling to an external antenna, and including various active elements into the sensor design that would condition incoming power and outgoing signal. Such miniaturized devices would also be useful in monitoring pressures within various other body compartments, so efforts are continuing on that front.

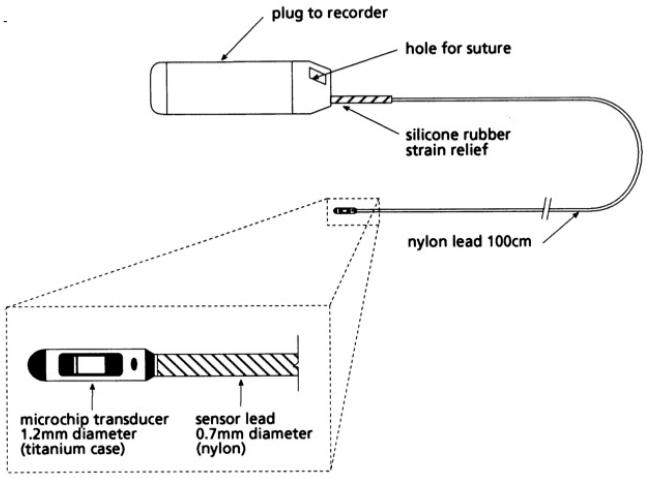

Figure 3 A microchip transducer.

From Peter Reilly and Ross Bullock, *HEAD INJURY Pathophysiology and management*

of severe closed injury, Fig. 10.5, P.213

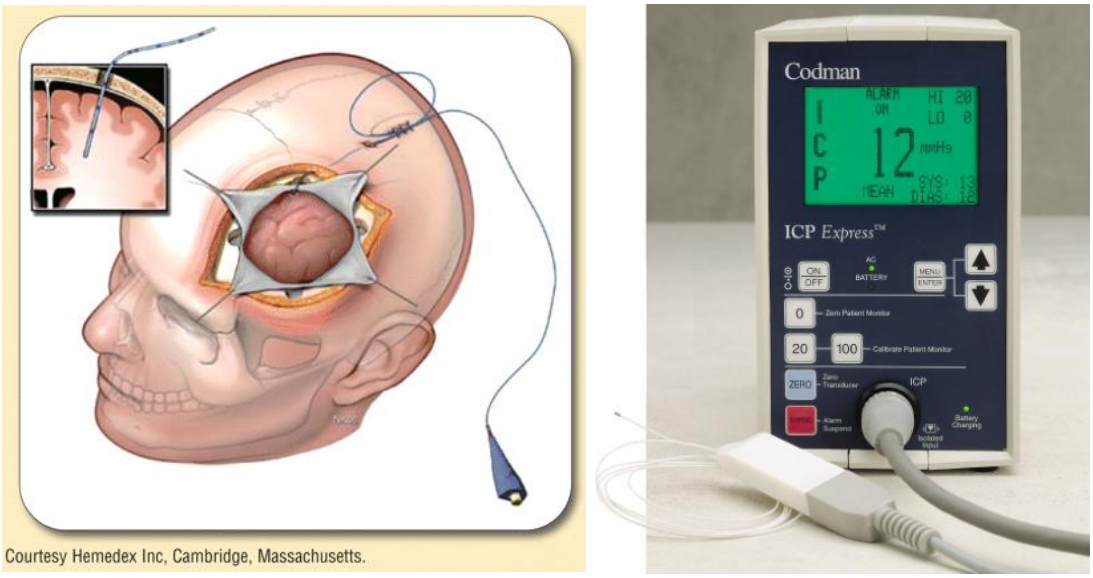

Figure 4: Codman ICP pressure sensor
From S. Cecil, P. M. Chen, S. E. Callaway, S. M. Rowland, D. E. Adler, J. W. Chen, *Traumatic Brain Injury Advanced Multimodal Neuromonitoring From Theory to Clinical Practice*, Crit Care Nurse April 2011 vol. 31 no. 2 25-37
and monitor from http://www.depuy.com

Telemetric ICP Measurement

Information about ICP is critical for treating hydrocephalus successfully and sustainably. It forms the decision making basis for guiding therapy. Implantable ICP monitors have also emerged with a catheter-tip transducer connected to a telemetry unit. Telemetric monitors are used for long-term monitoring of ICP in patients with hydrocephalus [9]. Telemetric ICP measurement is another invasive method with minimal risk of infection, reduction of inpatient treatment time and monitoring in an impatient setting. Besides, a telemetric catheter can be implanted for up to 3 months.

One available system consists of an implantable telemetric ICP probe (Neurovent-P-tel), a reading device (RAUMEDIC TDT 1 readP), a portable recording device including Universal Serial Bus port (RAUMEDICDataloggerMPR1) as shown in Figure 5, and a PC software for storing and analyzing data (RAUMEDIC Datalogger Vers. 1.7) as shown in Figure (6A). All devices were manufactured by Raumedic AG, Helmbrechts, Germany. The implanted telemetry ICP probe has a length of 25 mm and a thickness

of 1.76 mm; it consists of an intraparenchymatous pressure sensor at the end of the tip and a subgaleal transducer with a width of 31.5 mm in diameter and 4.3 mm thickness as shown in Figure (6B).

By evaluating the patient's ICP during normal activity, the shunt valve can be optimally adjusted for the patient's lifestyle, which significantly reduces the number of procedures on the patient's shunt valve [10].

Figure 5 Telemetric reading and monitoring device for ICP measurement. [10]

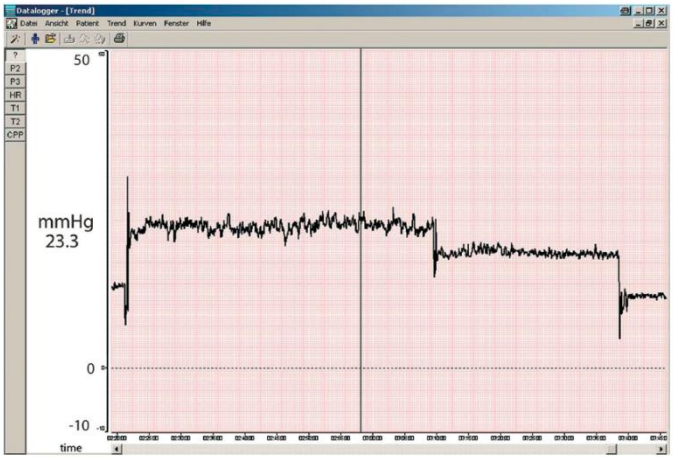

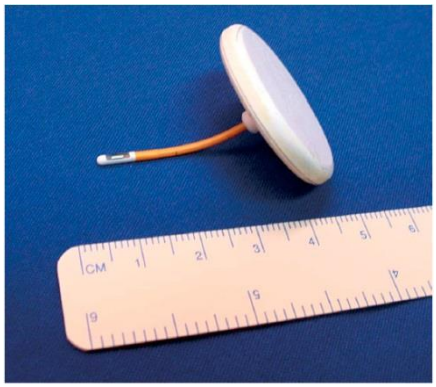

Figure 6 (A) Telemetric reading and monitoring device for ICP measurement**. (B)** Telemetric ICP probe, consisting of a ceramic body and a silicone coated catheter tip. ICP, intracranial pressure. [10]

In summary, the invasive methods for monitoring ICP share several common drawbacks as shown in Table 2. To realize the stability of pressure sensor zero drift, the sensor requires to be re-calibrated or replaced within the patient's body over time in some cases. Brain and spinal cord injury caused by inserting the sensor and frequent operations both increase the risk of complications. In addition, the insertion can be done only by a highly trained individual (neurosurgeon, or anesthesiologist in case of the spinal tap). In practice all three reasons lead to invasive ICP monitoring limited to neuro-intensive care units and specialized hospitals, and cannot be routinely used in general hospitals, emergency rooms, ambulatory settings or in the field [11].

In order to monitor the symptoms in hydrocephalus patients with conventional catheters, the patient must remain in bed. This is a significant disadvantage for the study of hydrocephalus. Monitoring ICP during movement and as the hydrocephalus patient changes their head position provides important insights into how to treat the symptoms.

Table 2. Methods for Invasive Monitoring of ICP [4]

Method	Advantages	Disadvantages
Intraventricular catheter	Provides 'true' global ICP Allows for CSF drainage and administration of drugs In-vivo calibration possible (external pressure sensor)	Infections Difficult insertion
Epidural catheter	Ease of insertion Minimal risk of infection (no penetration of dura)	Low accuracy
Lumbar CSF pressure	Extracranial procedure Can be performed ambulatory	May not reflect ICP Dangerous if ICP is very high
Catheter-tip micro-transducers (subdural or intra-parenchymal)	Rare complications during procedure Low risk of infections Can be made permanent implants	Drift of the transducer output over time In-vivo calibration not possible Inaccurate if intraparenchymal gradients exist

Noninvasive monitoring of intracranial pressure

The idea of measuring noninvasive ICP is attractive because complications in invasive ICP measurement methods such as hemorrhage and infection could be avoided. Also the insertion of a catheter or transducer is traditionally done only by a neurosurgeon in a specialized facility. In addition,

magnetic resonance imaging (MRI) can partially substitute for direct ICP monitoring for diagnostic information. Different techniques and methods have been proposed and developed.

Transcranial Doppler Ultrasonography

The TCD technique applies ultrasound to initially measure the blood flow velocity in the middle cerebral artery. The TCD measures the velocity of blood flow through the major intracranial vessels by emitting a high frequency (>2 MHz) wave from an ultrasound probe and detecting a frequency shift between the incident and reflected wave which directly correlates with the speed of the blood (the so called Doppler effect). The measurement is taken over the regions of the skull with thinner walls (temporal region, back of the head, or through the eye) as the bones strongly attenuate the transmission of the ultrasound at these frequencies as shown in Figure 7. ICP can be estimated from the TCD measurements because it impedes the blood flow and consequently decreases the velocity of blood flow.

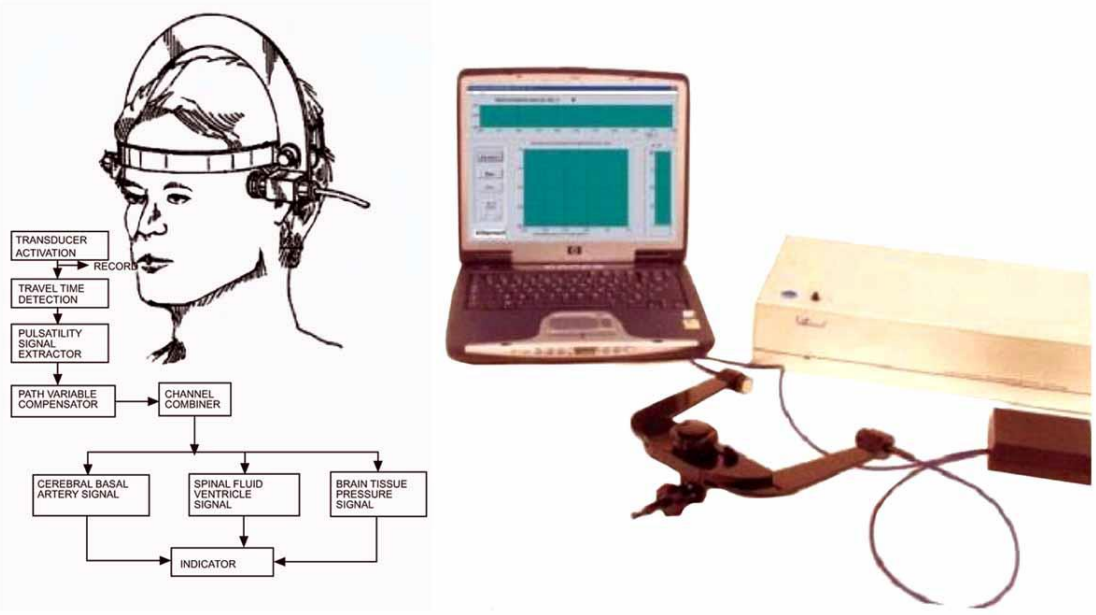

Figure 7(A) Schematic example of the time-of-the-flight ultrasound measurement. **(B)** Vittamed's system for noninvasive monitoring of ICP and intracranial slow, respiratory and pulse waves
From Djordje Popovic, Michael Khoo and Stefan Lee, *Noninvasive Monitoring of Intracranial Pressure.* Recent Patents on Biomedical Engineering 2009, 2, Fig.2 P.171

Magnetic Resonance Imaging (MRI)

The method of Alperin [12] as a noninvasive method of ICP measurement utilizes magnetic resonance imaging (MRI) as shown in Figure 8 and the intracranial pressure volume relationship in Figure (1B). MRI derives ICP from changes in intracranial volume that are calculated from arterial inflow, venous outflow and CSF fluid flow between the cranium and the vertebrospinal compartment. The blood flow is calculated from blood velocity, which is proportional to the phase difference between the incident and resonant radiofrequency signals, and cross-sectional areas of the main arterial and venous blood vessels which are obtained from static MRI scans. The average cost for each MRI scan is more than $1000 and the facilities are not flexible and portable. Therefore, an assessment of ICP based on repeated MRI scans would be inefficient, expensive, and potentially dangerous for the patient [13].

Electroencephalography (EEG)

Continuous ICP monitoring from the EEG is possible theoretically but difficult to achieve practically. The EEG can be recorded continuously at most for 8−12 h before the conductive gel on the electrodes dries off and the electrodes need to be replaced. In addition, continuous visual stimulation would certainly be fatiguing for conscious subjects. Also the accuracy of ICP levels from EEG signal is difficult to estimate. When the method was invented, the EEG was considered both sensitive and cumbersome for use in the dynamic settings of an emergency room, intensive care unit, or neurosurgery department. Recently, however, wireless, portable and field-deployable EEG systems [14] have become available and can be applied with ease by various medical personnel after minimal training.

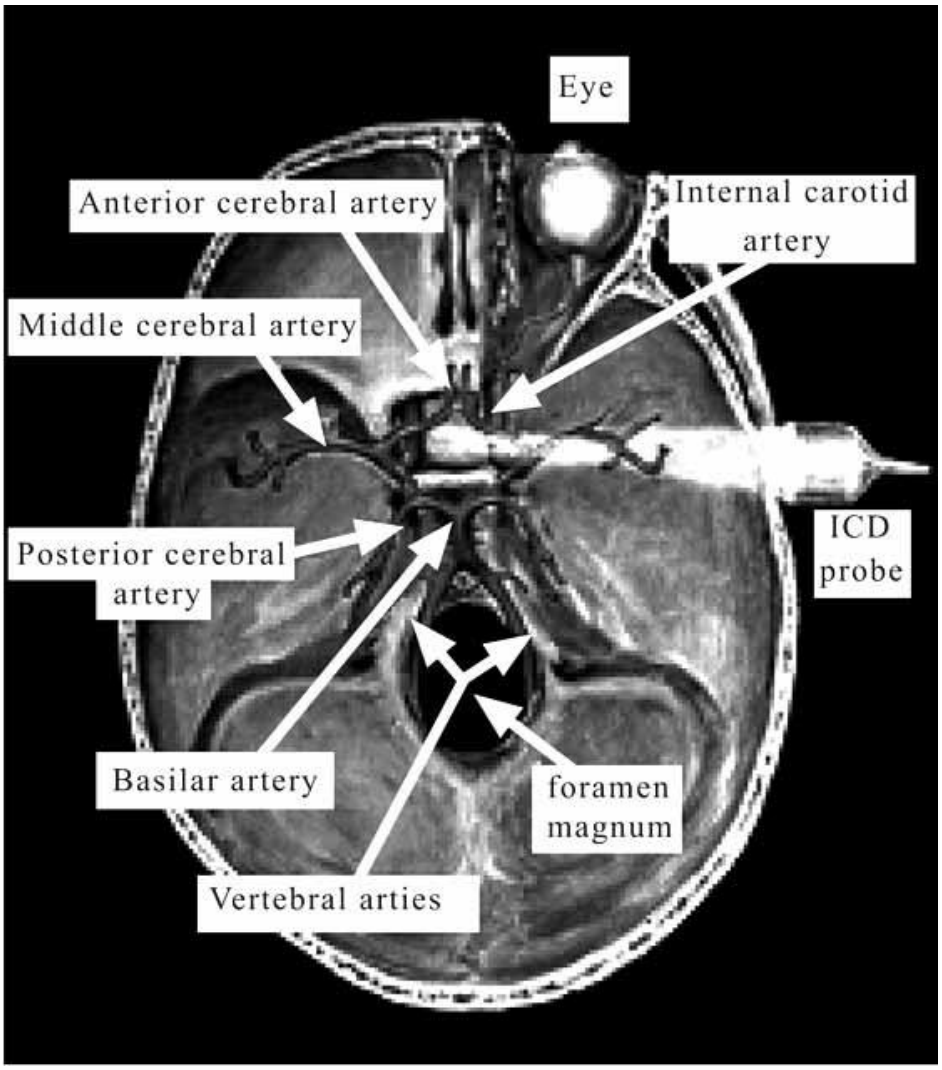

Figure 8 Transcranial Doppler ultrasonography of the cerebral circulation through the temporal bone

From Djordje Popovic, Michael Khoo and Stefan Lee, *Noninvasive Monitoring of Intracranial Pressure.* Recent Patents on Biomedical Engineering 2009, 2, Fig.3 P.171

In summary, the accuracy, skill level required for use, cost of technology, continuous monitoring and other advantages or drawbacks are shown in Table 3. The noninvasive methods for ICP monitoring are still in the exploratory phase because none of the methods are sufficiently accurate and easy to use at the same time. In addition almost all methods cannot be readily used for continuous monitoring of ICP so far.

Table 3. Comparison of Methods for Noninvasive Monitoring of ICP. [4]

Method	Accuracy (95% Conf. Intervals)	Skill Level Required for Use	Cost of Technology	Continuous Monitoring	Other Advantages or Shortcomings
Ultrasound time of flight	±20 mmHg [37]: ±9mmHg	Low	Moderate	Yes	Easily portable and field-deployable
Transcranial Doppler	±20 mmHg	Expert	Moderate	No	Finding correct vessels difficult even for experts
Acoustic properties of cranial bones	Not validated	Low	Low / moderate	Possible	Easily portable and field-deployable
EEG	Not validated	Moderate	Moderate	No	Repeated visual stimulation needed Cumbersome
MRI	Not validated	Expert	High	No	Not a bedside assessment
Tympanic membrane displacement	± 15-20 mmHg	Moderate	Low	No	Inapplicable in older patients
Otoacoustic emission	± 15-20 mmHg	Moderate	Low	No	Inapplicable in older patients
ONSD	± 5- 10 mmHg	Moderate/High	Moderate	No	
Ophthalmo-dynamometry	± 3- 5 mmHg	Expert	Low	No	Cumbersome
Jugular blood flow velocity measurement	Not validated	Expert	Low / moderate	No	Cumbersome Unpleasant

There are several methods either invasive or noninvasive to detect the intracranial pressure and hence CSF fluid accumulation. However, each of these existing methods has its own drawbacks. The catheter transducer method uses a ventricular (a set of structures containing cerebrospinal fluid in the brain) catheter and external transducer, which is not accurate and also exposes patients to high risk of infection [4]. In addition, most patients being monitored for ICP are likely to be suffering from head injury and they will usually have narrow ventricles, making ventricular surgery more difficult. Magnetic resonance imaging (MRI) method is a non-invasive method to detect abnormal accumulation of CSF fluid. However, MRI is expensive and not portable. The patients must go to MRI facilities for examination. The Codman ICP sensor [4] uses a strain gauge to measure ICP pressure directly inside the brain. Changes in ICP pressure are sensed as changes in the sensor resistance. However, the Codman ICP sensor can only be kept in place/brain for a maximum of two weeks in order to avoid infection and other complications due to external wiring through the skin [15].

The future of the field will take into consideration the cost, accuracy, ease of use and continuous monitoring ability at the same time. Commercial research is also headed to design a passive sensor, which could be permanently implanted to ensure accuracy.

The goal of our research is to design a permanently implantable passive pressure sensor to provide constant monitoring of the ICP pressure, which meeting all the future requirements. Our research has been focused on creating a passive, wireless sensor that can be implanted for 10 or more years, that off-loads the complex processing into an external reader, keeping the sensor element itself simple and therefore less likely to fail. The cost of each sensor can also be kept low, because creating the necessary circuit elements is much easier without the space constraints. This sensor will be inserted through the protective layer covering the brain, a location known as Dura mater. After surgery, repeated measurement can be performed at the bedside. The ICP pressure can be read out wirelessly using a hand-held external reader. Wireless telemetry reduces the risk of infection and inconvenience of external wires. The reader will display the internally measured ICP and waveform to facilitate real time assessment of the patient's condition by the clinician. A physician will be able to receive the pressure readings for early detection of shunt failure; as well as to help patients avoid unnecessary shunt revisions.

An external reader will emit a radio signal that sweeps over the range of the possible resonant frequencies of the sensor. The reader will consist of a voltage-controlled oscillator (VCO) controlled by a microcontroller and digital to analog converter (DAC). The measurement is through inductive coupling much like a transformer. When the sweeping frequency approaches the resonant frequency, the resonant tank circuit will behave as a high impedance load, allowing accurate estimate of the resonant frequency. Using calibration curves, the ICP value may be inferred from the measured resonant frequency.

Summary of desired technical capabilities:

- Pressure range: –30 to 100 mmHg
- Drift: 1 mmHg/year
- Sensitivity: at least 0.1 mmHg
- Sampling rate: 100 Hz or more (prefer to capture nearby arterial pressure pulsations)
- Keep accurate measurements regardless of ambient pressure changes (for example elevation)
- Able to be removed in one piece if necessary
- Biocompatible

Surgery Specifications

In order to reach the brain during surgery, surgeons need to cut through three layers, the scalp, the skull, and the Dura. The scalp can have variable thickness, but on average is 10 mm. The skull can also have variable thickness, depending on age, and can range from 10–20 mm. The Dura is usually 1–3 mm thick and is a leathery layer underneath the skull.

Currently, Codman intracranial pressure sensors are used to measure ICP in a hospital setting. The Codman sensor consists of a diaphragm and a Wheatstone bridge circuit. The diaphragm is at the tip of a long, 3 mm diameter tube that needs to be surgically implanted into the brain and snaked to a separate reader. The sensor can only be kept in place for a maximum of two weeks in order to avoid infection and other complications due to external wiring through the skin [15].

After the path to the brain is created, the Codman pressure sensor is inserted through the slit in the Dura. The diameter of the tube is 3 mm, allowing the sensor to easily fit. An 18 mm diameter titanium cap is then placed on the skull and screwed into place with two 7 mm brain screws. The cap prevents the sensor from moving or slipping out [15].

The surgical procedure to implant our ICP sensor would be similar to that of the current surgical method of cerebral shunt and Codman sensor implantation.

The surgeon begins by making three incisions on the scalp, in order to peel the scalp from the skull. Once the skull is revealed, a bone drill is used to drill a 10–14 mm diameter hole through the skull. Lastly, a 5 mm slit is made in the Dura in order to reach the brain. Our ICP sensor will fit through the drilled hole and the 5 mm slit.

Based on the current surgery, our ICP sensor will need to fit through the 5 mm slit in the Dura in order to reach the brain. The holder of the sensor will need to fit within the 10–14 mm diameter hole in the skull, and should have a similar securing method with 7 mm screws. Also, it would be preferred to have room to fit a catheter or shunt of 3 mm past the holding device. Since the skull can have varying thicknesses, the stem of the holder will need to come in variable lengths to match each specific patient.

Early Work of sensor concept proof

The earliest proof of concept system was developed by Dr. Josh Medow on a breadboard and included a basic tank circuit to simulate a potential sensor, with a corresponding inductive receiving element to provide power to the device at the same time as reading the data output. Back in 1967, Collins also published a paper on a miniaturized, implantable intraocular pressure sensor that combined the inductive and capacitive elements of the basic tank circuit and utilized the grid dip meter concept of wirelessly measuring the resonant frequency of *LC* circuits. Based on these two ideas large scale prototype device was developed as proof of concept shown in Figure 9.

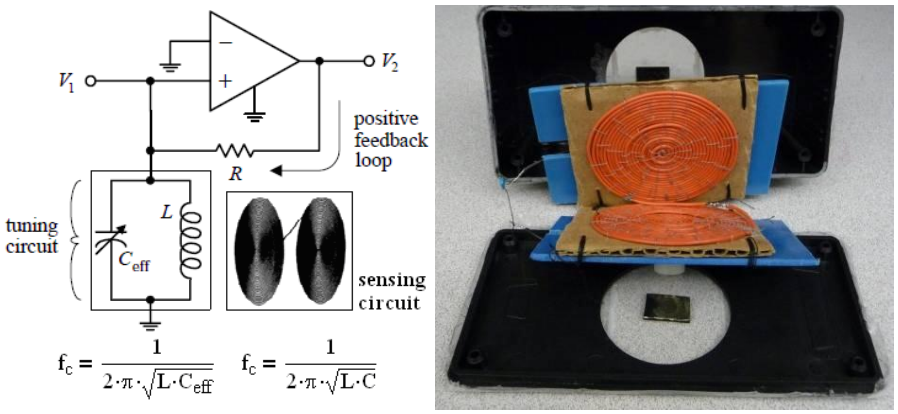

Figure 9 (A). System overview. **(B).** Open view of the large scale prototype sensor

The two coils formed a two-part inductor necessary for inductive coupling to an external antenna. When assembled, they would face each other directly with a very small gap separating them. Assembly was accomplished by sewing 14 gage insulated wire onto a cardboard substrate for stability. The capacitance and inductance of this system would change based on the distance between the coils.

Then a smaller scale prototype of the sensor was created as shown in Figure 10. This involved creating a different oscillator capable of higher frequencies to match the increased resonant frequency of a smaller sensor - with smaller sensor size the inductance and capacitance are both reduced. A test of coil spacing changing influences the resonant frequency changing.

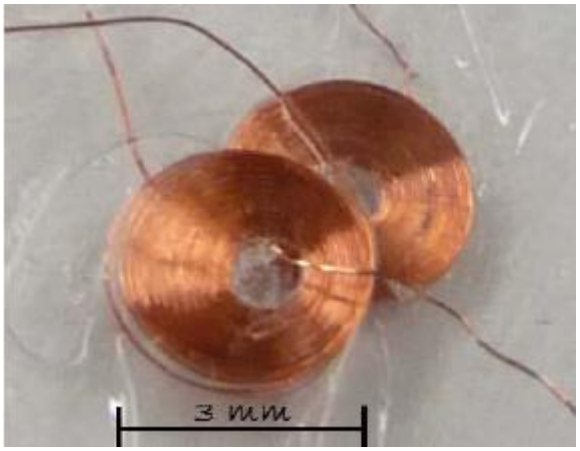

Figure 10 small scale prototype sensor

In this small scale prototype, two round plates from clear plastic were created. Each round plate had a drilled hole in the center. Then a piece of transparent round shape was attached but with slightly

larger diameter to reduce the amount of potential wire snagging. The transparent round shape formed the coil spool, while the reusable round plate created a stable background for winding. In order to create coils, 44 gauge wire was passed through one of the holes and wound 25 turns around the spool through the center holes to create a coil set with an inductance of 0.5 µH, and a capacitance of 2 pF. The resonant frequency was around 120 MHz, depending on coil-coil distance, and the oscillator was able to pick up the coil from about 3 cm away. Water soluble glue applied kept the coil wire from unwinding later. The spool was removed as soon as the winding was done and the coils were allowed to dry.

Current approach of Sensor Design

The implanted ICP pressure sensor is a micro-electro-mechanical (MEM) sensor that transforms variation of pressure to variations of the resonant frequency of a variable *LC* tuner. Referring to Figure (11A), the sensor assembly consists of a glass substrate and silicon on insulator (SOI) membrane acting as a diaphragm. The SOI was etched to allow placement of two metal layer plates separated with a gap filled with vacuum insulation. When implanted in the brain, ICP deforms the membrane, reducing the gap between the two metal plates, and changing the capacitance. Each metal plate was etched into a planar coil inductor connected at one end. This leads to an equivalent *LC* circuit as shown in Figure (11B). This is known as a resonant tank circuit [16]. Changing the gap spacing due to ICP pressure causes changes of the corresponding capacitance, and hence the natural resonant frequency and the quality factor *Q*. Here qualify factor *Q* is a dimensionless parameter that describes/characterizes a resonator's bandwidth relative to its center frequency [17].

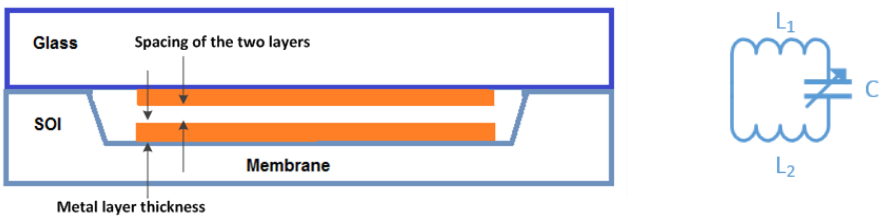

Figure 11 (A). Front view of sensor fabrication structure. **(B).** Equivalent circuit representation of the sensor

The overall structure was also restricted in terms of geometry and orientation. A geometry limitation on the sensor is the range and overall transmitting/receiving power of the inductor. If the coils are too small, the range to the external reader may not be large enough to carry the signal and power a long enough distance. At the same time, the capacitance needs to be reasonably matched to the inductance to create a balanced tank circuit (as mentioned in the previous section).

Ideally, based on mathematical simulations (done and documented by Gerhard van Baalen), the coils need to be interconnected to double the inductance and increase the quality factor *Q*. At the same time, the resistance of the tracks needs to be low. These two ideal goals are challenging in terms of sensor fabrication in the clean room. A higher *Q* is desirable for a higher precision, as the resonant frequency matching effect of reader and sensor will be much sharper and well defined. For these reasons, our current test wafers contain 6 different sensor geometries for further testing and optimization.

Building a prototype of the MEM-based sensor is a major challenge of this project. To realize the tiny size and make sure the accuracy, the sensor can only be manufactured inside a cleanroom. To create a tiny, implantable sensor, the process involves etching a cavity in silicon, laying down a metal coil, and bonding another wafer with a metal coil on top.

Only crystalline structures offer the minimal drift properties over time that our application necessitated. The most commonly used, cheapest single crystal material with very well defined processing techniques is of course silicon. This material is chosen as our membrane because it is possible, using micro fabrication techniques in the cleanroom, to pattern metal structures and to create a large capacitance by minimizing the distance between the coils to the order of micrometers. The materials chosen for fabricating this sensor are silicon, glass and copper. Silicon and glass are crystal with dimensional stability, and copper has low resistivity and high conductivity. Also as Figure (11A) shows, the pressure sensing cavity is carved out of the silicon part of the assembly, since silicon etching methods

produces a perfect surface suited for metal deposition. Glass was chosen as the second component for two reasons: 1) It takes fewer steps and is more accurate to align the two halves when one of them is transparent and 2) The most reliable way to bond the two together and create a vacuum cavity is anodic bonding, which is a bond between silicon and glass.

In addition, to create the thin pressure membrane, the starting material must be an SOI (Silicon on Insulator) wafer. This type of wafer has a thick handle (in our case 500 μm), and a thinner device layer (in our case 100 μm) separated by a SiO_2 layer (the insulator layer). It is a very common approach in the fabrication of pressure sensing cavities, because it allows for precise control of the device layer, and because the separating insulator layer provides an etch stop when removing the handle. Otherwise, it would be completely impractical (in terms of cost and mechanics) to work with specific thickness thin wafers that have specific thickness membrane patches.

In order to reduce resistive loss between the tracks, the device layer Si must have a low level of dopant to raise its intrinsic conductivity. Our test wafers match this property fairly closely, and are also 625 μm thick to approximate the SOI wafer thickness. Additionally, most tools in Wisconsin Center for Applied Microelectronics (WCAM) currently work with 4 in (100 mm) wafers, thus determining our wafer diameter. Finally, the crystal plane orientation is such that the <100> plane is at the surface (one of the most common configurations, and important for selective wet etch purposes). Current specs of our wafers are summarized in Table 4.

Table 4. Comparison properties of different wafers

Property	**SOI wafers**	**Glass wafers**	**Si test wafers**
Diameter	100 mm/4 in	100 mm/4 in	100 mm/4 in
Dopant/type	Boron (P-type)	Borofloat	Boron (P-type)
Orientation	<100>	n/A	<100>
Resistivity	100-200 Ω cm	n/A	30-50 Ω cm
Flats	Dual	Dual	Dual
Finish	Double sided polish	Double sided polish	Single sided polish
Thickness device layer	107 μm	500 μm	625 μm
Thickness thermal oxide	1 μm	n/A	n/A
Thickness handle	500 μm	n/A	n/A

Note that there is a distinct difference between glass wafers and fused quartz wafers (not shown in table). Fused quartz wafers are amorphous SiO_2 and are allowed to be used in most tools, whereas glass wafers contain impurities that make them conductive and suitable for anodic bonding, but can introduce contamination detrimental to users creating transistors and related things in the clean room. Fused quartz wafers are only used as carriers and are not part of the actual sensor structure, as described further below.

Any patterns on the wafers are created by using photoactive polymers called photoresists (PR). The pattern to be transferred is captured on a mask – a square piece of glass coated with a thin layer of Chromium that blocks the transmission of ultraviolet light. Ultraviolet (UV) light exposing positive photoresist removes anything that got exposed to the light, transferring the pattern you see on the mask directly onto the wafer. Negative photoresist reacts exactly the opposite, and stabilizes upon light exposure, so that the pattern transferred is always the inverse of what is on the mask. Some unique image reversal photoresists can be persuaded to behave either as positive or negative, depending on the process conditions. The one I have used started as positive PR, but upon further baking and exposure reverses to a negative photoresist. A developer then washes away leftover photoresist and creates the final pattern – typically the developer is specific to the photoresist used, as it is optimized to perform the best for that particular PR. Table 5 shows a summary of photoresists used in the fabrication of the sensor – note that some of these properties change if a deviation from the currently used recipe is introduced. Recipes currently used can be found in the appendix.

Table 5. Different photoresist parameters comparison summary

Photoresist	Type	Typical thickness	Developer	Exposure time	Typical application
1813	Positive	1-1.5 μm	MF-321	7-7.5 s	Generic
1827	Positive	2.5-3 μm	MF-321	25-28 s	Liftoff
SPR 220-7	Positive	10-15 μm	MF-24A	20-30 s	Liftoff thicker layers
Intervia BPN	Negative	20+ μm	Intervia BP	85-100 s	Electroplating
AZ 5214	Either	1-2 μm	AZ 327	8 s + 10 s	Image reversal

Current approach of sensor concept proof

Deflection

Based on the dimensions of the sensor, the thickness of the diaphragm can be determined to maximize sensitivity. The diaphragm, or the bottom wafer, is 3 mm wide and 6 mm long, with 3 µm of possible deflection space. The material is silicon, which has an elastic modulus of 30 GPa and Poisson ratio of 0.28 [18]. The deflection can be calculated using the rectangular deflection equation [19];

$$D = \frac{E \cdot h^3}{12 \cdot (1 - v^2)}$$

$$y = \frac{b \cdot p \cdot a^4}{D}$$

Where, E is the elastic modulus, h is the height, v is the Poisson ratio, b is 0.00254 (for rectangle of side a by $2a$), p is the pressure, and a is the small side length. Choosing a to be 3 mm, the deflection at the maximum pressure of 860 mmHg is shown versus height in Figure 12.

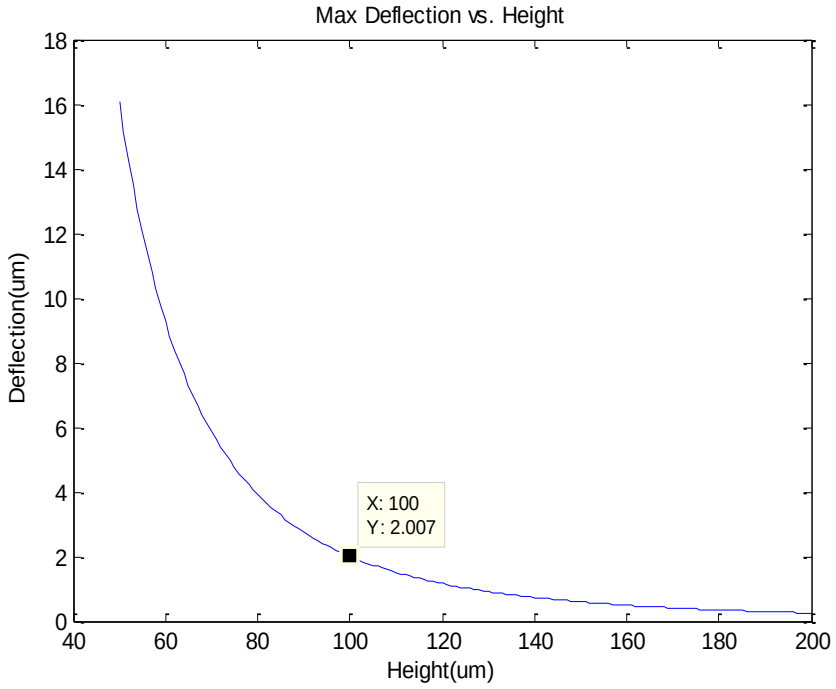

Figure 12 Deflection versus height of a 3 mm x 6 mm silicon diaphragm at 860 mmHg pressure.

A deflection of 2 μm was chosen in figure 3 to ensure that the inductor coils never touch since they start with a 3 μm separation. In order to achieve different value of deflection, the membrane needs to have corresponding thickness. In figure 3 to achieve 2 μm of deflection, the membrane needs to be 100 μm thick. Also to achieve around 40 μm of deflection, the membrane needs to be 60 μm thick. From the simulation result, the max deflection distance of the silicon membrane is about 40 μm in the ideal situation and the space between the two metal layers should be as least 40 μm to avoid touching of the two metal layers. However, in the real situation, we usually can not realize such a large distance because of the constraints of the real experiment environment.

To understand the shape of the deflection across the entire diaphragm, the sensor was modeled in SolidWorks with two layers: one layer is silicon with an area 4 mm × 7 mm and thickness 60 μm and the other layer is copper with area 3 mm × 6 mm and height 55 μm. The boundary of the model is fixed and the pressure is set at 860 mmHg to simulate the environment of the human brain. Table 6 shows the copper and silicon properties used in SolidWorks software.

Table 6 (A). Silicon and Copper material properties used in software (Copper property)

Property	Value	Units
Elastic Modulus	1.1e+011	Pa
Poissons Ratio	0.37	N/A
Shear Modulus	4e+010	Pa
Density	8900	kg/m^3
Tensile Strength	394380000	Pa
Compressive Strength in X		Pa
Yield Strength	258646000	Pa
Thermal Expansion Coefficient	2.4e-005	/K
Thermal Conductivity	390	W/(m·K)

Table 6 (B). Silicon and Copper material properties used in software (Silicon property)

Property	Value	Units
Elastic Modulus	1.124e+011	Pa
Poissons Ratio	0.28	N/A
Shear Modulus	4.9e+010	Pa

Density	2330	kg/m^3
Tensile Strength in X		Pa
Compressive Strength in X		Pa
Yield Strength	120000000	Pa
Thermal Expansion Coefficient		/K
Thermal Conductivity	124	W/(m·K)
Specific Heat		J/(kg·K)

We should ensure that the yield strength and tensile strength of Copper and tensile strength of Silicon are satisfactory. The values are 394,380,000 Pa 258,646,000 Pa and 120,000,000 Pa separately.

Figure 13 shows the results of the deflection simulation when the pressure is 860 mmHg. The maximum deflection matches the calculated deflection, and it can be seen that the deflection is greatest in the middle of the long rectangular patch. The maximum deflection is 2.32 μm, which is kind of small compared with thickness of the materials and far smaller than the value of the ideal situation. Figure 14 shows the results of the stress simulation result when pressure is 860 mmHg

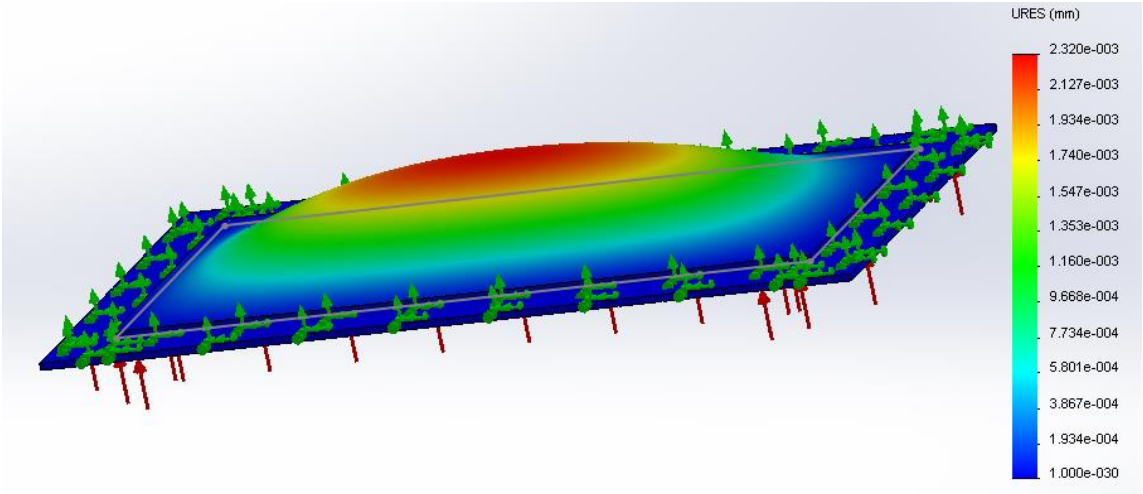

Figure 13 deflection simulation result when pressure is 860 mmHg

The maximum stress is 56,888,696 Pa and in Figure 13 the average stress is around 20,000,000 Pa which is smaller than the stress strength value (394,380,000 Pa 258,646,000 Pa and 120,000,000 Pa). The stress simulation result in Figure 14 shows that no worry is needed about the stress problem

between Copper and Silicon as previously concerned. According to this simulation, the stress and recovery deformation of the copper won't be a problem even when the thickness of the copper substantially increases to realize the resonant frequency property (such as 55 µm).

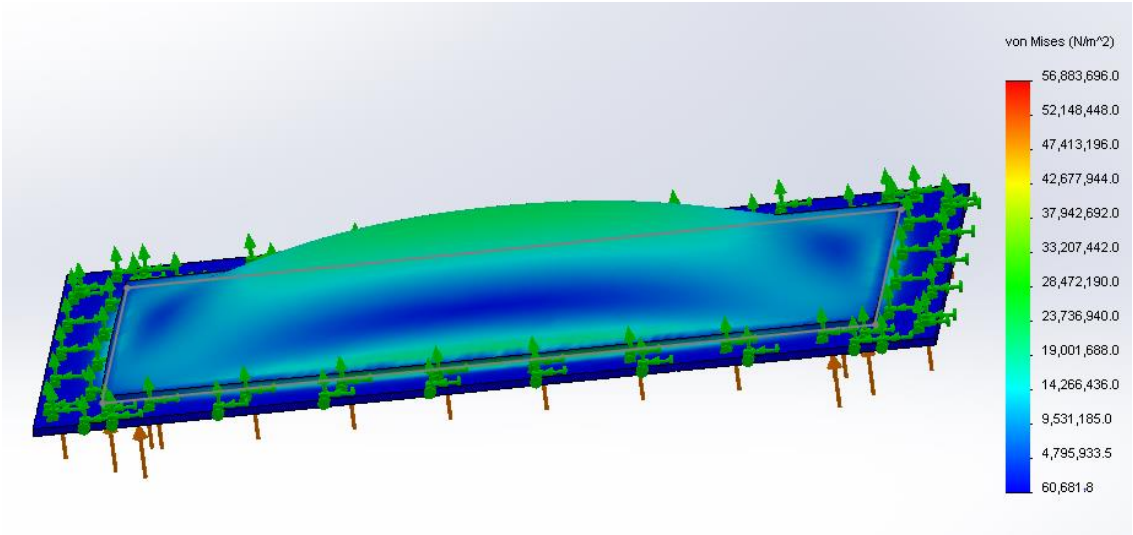

Figure 14 Stress simulation result when pressure is 860 mmHg

With the diaphragm chosen to be a specific thickness, it is possible to plot the separation of the coils versus pressure and give an idea of the sensitivity of the sensor. Figure 15 shows the plot of separation versus pressure with the inductors starting 3 µm apart at 0 mmHg when the diaphragm is 100 µm. With the chosen sensor dimensions, the separation changes 2.3 nm per mmHg.

Coil Design

The electrical characteristics for the sensor that need to be considered are the capacitance, inductance, resonant frequency, and quality factor. All of these characteristics should be maximized and are very dependent on the size of the sensor.

The capacitance of the sensor can be predicted using the equation [20]:

$$8.85 \times 10^{-12} \cdot \frac{A}{s}$$

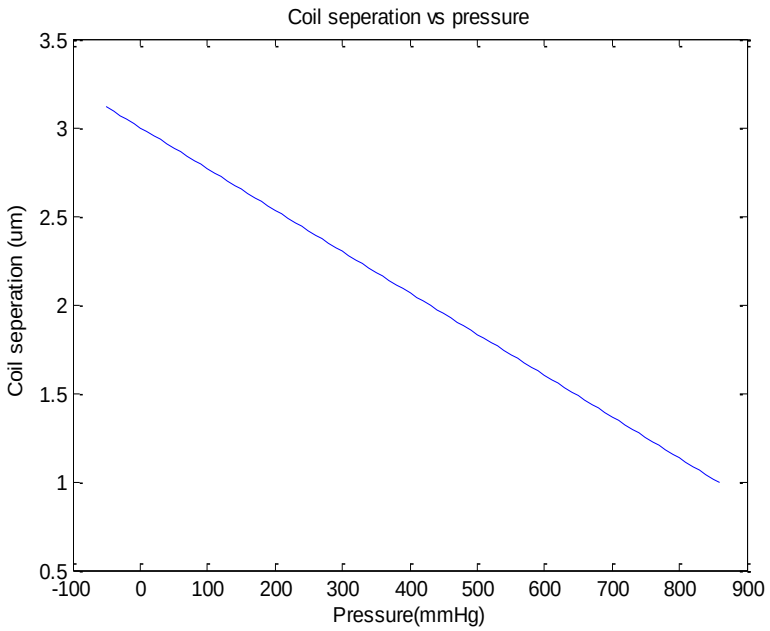

Figure 15 Separation of the two inductor coils versus pressure

Where *A* is the area of the conductive plate and *s* is the separation between the conductive plates. The capacitance can then be estimated easily by assuming an area of 3 mm × 6 mm and a separation of 3 mm to 1 mm from the deflection equations. Figure 16 shows the capacitance versus pressure for the 3 mm × 6 mm sensor starting at a separation of 3 µm, and deflecting 2 µm.

The inductance of the sensor is much more difficult to predict and is dependent on the self-inductance and mutual inductance. The total inductance of the system, approximated as two coupled inductors, can be written as [20]:

$$2L \pm 2M$$

Where *L* is the self-inductance of one coil and *M* is the mutual inductance between the coils. Mutual inductance is dependent on the distance between the coils, and therefore changes just like the capacitance as the pressure changes. However, the change in mutual inductance over the 2 µm deflection is negligible, and is considered constant. The Matlab program was created to verify the inductance predictions [21].

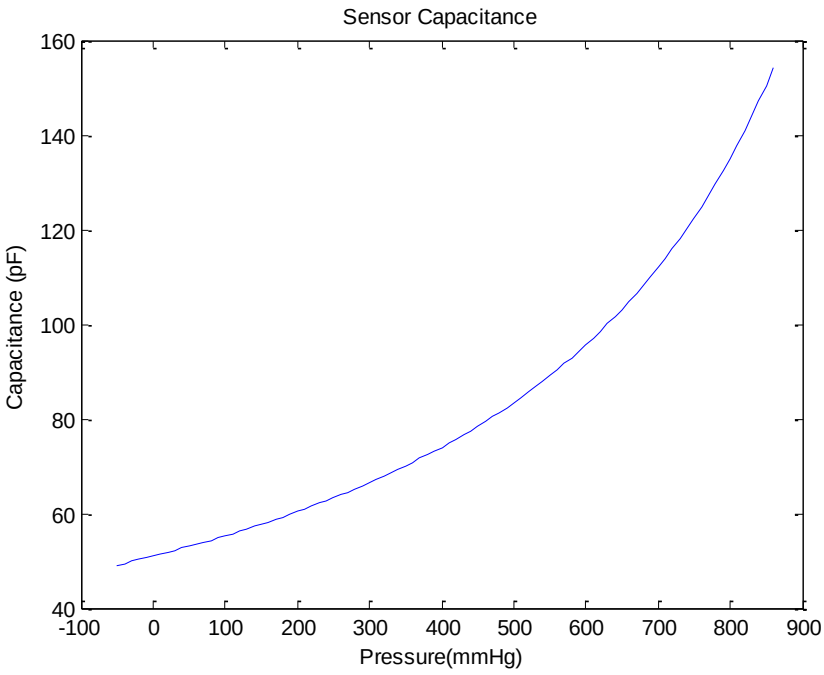

Figure 16 Capacitance versus pressure for the proposed sensor.

The resonant frequency of the system can be predicted from the capacitance and inductance of the sensor with the equation [22]:

$$f = \frac{1}{2\pi\sqrt{LC}}$$

Where *f* is the resonant frequency, *L* is the total inductance, and *C* is the capacitance.

The last characteristic, the quality factor, describes how well the senor resonates, or how sharp the resonant peak will be. In general, a high quality factor is ideal for sensor resolution and ease of detection. The quality factor can be calculated as [22]:

$$Q = \frac{\sqrt{\frac{L}{C}}}{R}$$

Where *Q* is the quality factor, *L* is the total inductance, *C* is the capacitance, and *R* is the resistance. From previous studies, a quality factor of around 15 is sufficient for distinct resonant peak detection [23]. Of concern in the sensor design is the resistance, since the maximum height of the metal tracks on the

sensor is 2 µm due to clean room specifications. Therefore, for coil design, the width of the tracks was increased to reduce resistance.

Since the capacitance of the sensor is maximized based on the sensor size, the inductance of the sensor needs to be carefully considered for coil design. Inductance should be maximized, because the greater the inductance, the greater the signal strength of the sensor when measuring resonant frequency and the greater the distance away a measurement could be made. However, to increase the inductance, the number of turns needs to be increased. Since the area for the turns is limited to 3 mm × 6 mm, to increase the number of turns, the track width needs to decrease. Decreasing the track width increases the resistance of the sensor which greatly reduces the quality factor, making it impossible to detect the resonant peak. Therefore, the inductance was maximized while keeping the quality factor around 15.

For the first design iteration, six different types of coils were tried. Half of the designs used a solid plate in the center, with coils around the plate. This reduces the resistance, increases the capacitance, and has little effect on the inductance. Since the deflection of the rectangular membrane is greatest in the center, a solid capacitive plate in the center maximizes the change in capacitance. Also, the outer turns of an inductor add most to the inductance, and therefore removing the inner most turns does not change the inductance significantly. The other half of the designs are planar coils, to optimize inductance. Of note for the first design iteration, the coils were assumed to be able to be connected together and therefore resulting in the system of inductance described by the equation

$$L_{\text{total}} = 2L \pm 2M$$

The inductance is doubled since the inductors are in series. Not connecting the two inductors assumes to reduce the total inductance to half the self-inductance of one coil plus the mutual inductance. This is because the inductors are now in parallel.

$$L_{\text{total}} = \frac{1}{2}L \pm 2M$$

The relationship between the system inductance and the inductance of a single coil was proven using CST Microwave Studio and then experimentally. A large scale sensor was created with a single coil inductance of 600 nH. The system inductance with two connected coils was simulated and measured to be 1260 nH while the system inductance with two unconnected coils was simulated and measured to be 365 nH.

Finally, of importance is the resistivity of the silicon substrate the inductor coils are bonded to. If the silicon is not insulating enough, current from the coils can leak through and short the sensor. The resistivity of silicon is 300 Ωmm, while the resistivity of gold is 2.44*10^-5 Ωmm [18]. With a cross sectional area of 3 mm × 100 µm, and a length of 6 mm, the resistance can be calculated by the equation

$$R = \frac{\rho l}{A}$$

Where ρ is the resistivity, *l* is the length, and *A* is the cross sectional area. The resistance of the silicon is then 6 kΩ, which is much higher than the resistance of the sensor.

The specific geometries of the different coil designs are shown below. Each coil has different track widths and number of turns. This changes the inductance and resistance of the coils. For every design, the gap between the tracks was kept at 20 µm, which keeps the capacitance about the same between all of the designs since there is little open space.

Coil 1

The first coil design uses the center capacitive plate idea with surrounding inductor tracks. The spacing between tracks in minimized in order to keep the inductor area large and approximate a solid capacitive plate. Figure 17 shows the design of coil 1.

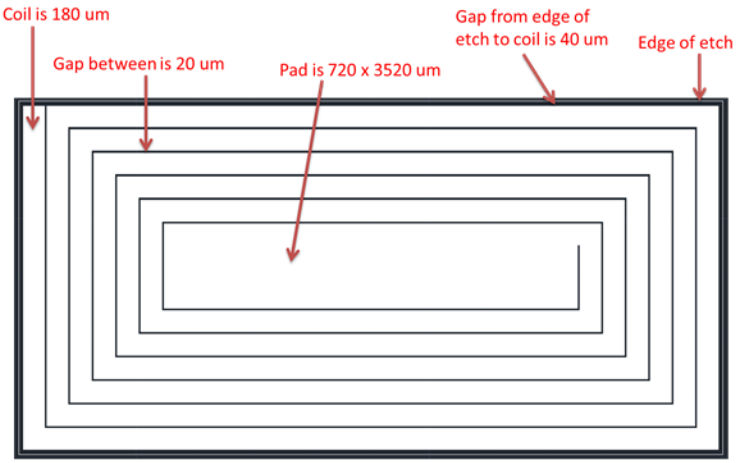

Figure 17. Coil design 1

Coil 2

The second coil design followed the first, but changed the area of the solid capacitive plate. Increasing the area of center capacitive plate reduces the resistance, allowing for thinner inductive tracks, which can increase the number of turns and the inductance. Figure 18 shows the design of coil 2.

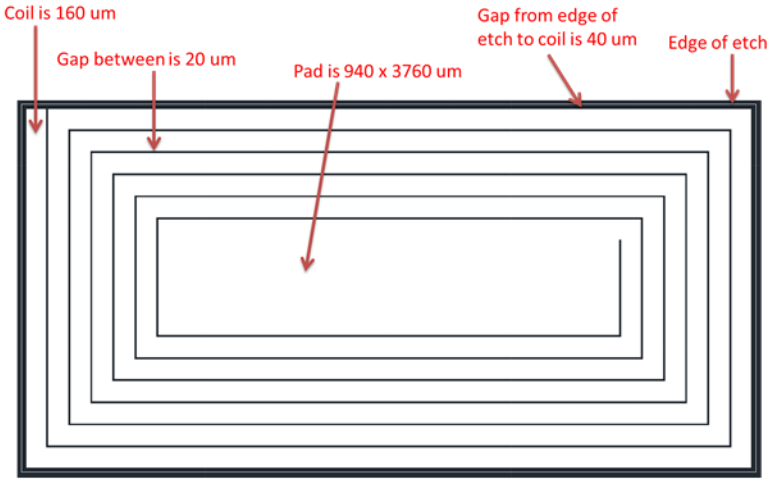

Figure 18. Coil design 2

Coil 3

The third coil design also continues the design for coil 1 and 2 by increasing the size of the capacitive plate even more. Figure 19 shows the design for coil 3.

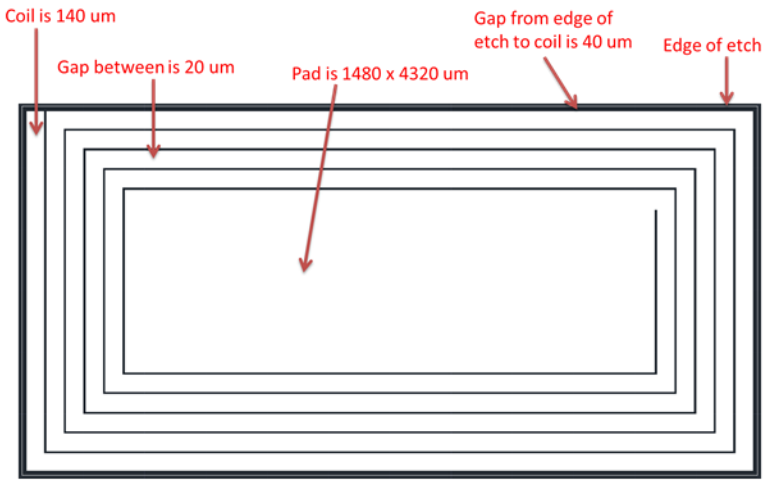

Figure 19. Coil design 3

Coil 4

The design for coil 4 does not use a capacitive plate and is simply an inductive track. Designs of this type maximize inductance over capacitance since there are more turns. This specific design also tries a method for connecting the two coils when they are bonded together. The metal of the coil extends to the edge of the etched cavity, which overlaps the area that is bonded. Therefore, the two metals will be in contact when placed together. Figure 20 shows the design for coil 4.

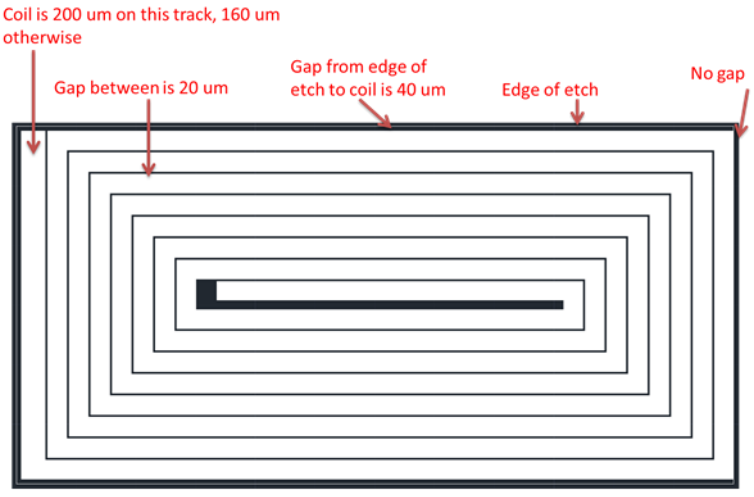

Figure 20. Coil design 4

Coil 5

The design for coil 5 matches exactly to coil 4, except the metal track does not extend to the edge. When this coil is bonded together, the coils are not connected. Figure 21 shows the design for coil 5.

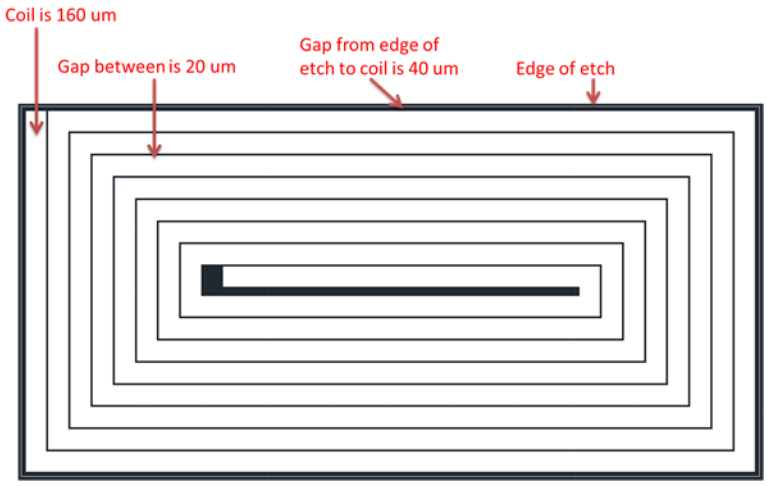

Figure 21. Coil design 5

Coil 6

Finally, for the sixth coil design, the inductance made as large as possible while ignoring the resistance and quality factor. This was done to test the effects of the quality factor on the measurement of resonant frequency. Figure 22 shows the design for coil 6.

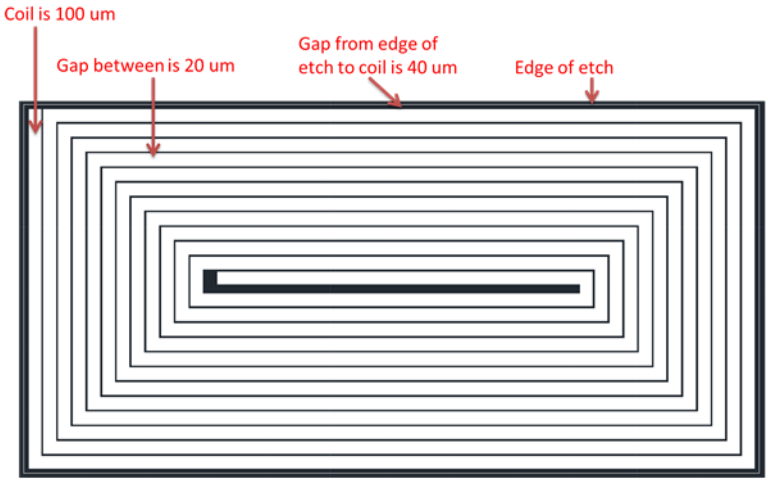

Figure 22. Coil design 6

The electrical characteristics for each coil design were calculated using the methods described previously. A Matlab program was created to perform all the calculations and graph the results. Table 7(A) summarizes the characteristics for each coil over the range –50 mmHg to +860 mmHg pressure for connected systems, Table 7(B) summaries the characteristics for unconnected systems. The resonant frequency, which is the parameter for measurement, changes approximately 20 - 40 kHz per mmHg. This is essentially the resolution of the sensor, and should be as large as possible.

Table 7 (A). Table summarizing the electrical characteristics of each design as a connected system. The ranges are over the pressure -50 to 860 mmHg

Coil Type	Inductance Single Coil (nH)	Inductance (nH)	Capacitance (pF)	Resonant Frequency (MHz)	Resistance (Ω)	Quality Factor
1	135	270	45 – 150	45 – 24	10.16	15.2 – 8.8
2	160	320	45 – 150	42 – 23	11.77	14.0 – 8.0
3	153	306	46 – 152	42 – 23	11.90	13.6 – 8.0
4	170	340	43 – 145	41 – 22	14.65	12.0 – 6.8
5	170	340	43 – 145	41 – 22	14.65	12.0 – 6.8
6	400	800	41 – 136	28 - 15	35.20	8.0 – 4.4

Table 7 (B). Table summarizing the electrical characteristics of each design as an unconnected system. The ranges are over the pressure -50 to 860 mmHg.

Coil Type	Inductance Single Coil (nH)	Inductance (nH)	Capacitance (pF)	Resonant Frequency (MHz)	Resistance (Ω)	Quality Factor
1	135	70	45 – 150	91 – 50	10.16	7.6 – 4.4
2	160	80	45 – 150	84 – 45	11.77	7.0 – 4.0
3	153	78	46 – 152	85 – 47	11.90	6.8 – 4.0
4	170	85	43 – 145	82 – 45	14.65	6.0 – 3.4
5	170	85	43 – 145	82 – 45	14.65	6.0 – 3.4
6	400	200	41 – 136	55 – 30	35.20	4.0 – 2.2

Connecting the coils gives the greatest inductance and quality factor, but is difficult to do in fabrication. Therefore, unconnected coils were attempted at first. With a lower inductance, the range of detection decreases, but the resolution increases since the resonant frequency is more dependent on the changing capacitance. This may allow resonant frequency detection even at lower quality factors.

Clean Room Processing

The final step of coil design was to create an AutoCad layout of each of the coils for clean room processing. Two masks had to be made, one to etch the silicon for the sensor outline, and the other one to place the metal tracks.

The etch mask has the 3 mm by 6 mm wells for the metal coils to fit in. The wells are spaced 1 mm apart on all sides. There are cut marks placed between the wells to ensure a straight slicing. When the coils are sliced, the final sensor is 4 mm by 7 mm since there is an extra 0.5 mm on all sides. Again, this space is for the anodic bonding process. The etch mask is shown in Figure 23.

Of importance for the coil mask, is the symmetry of the coils. When two of the coils are put together to make a sensor, the direction of the turns have to be opposite, i.e. one coil must be wrapped clockwise, while the other is counterclockwise. This is so current can flow continuously though the two coils and the mutual inductance will add to the overall inductance. Otherwise, the inductance would subtract, lowering the inductance. Therefore, a horizontal line of symmetry was created in the middle of the mask. If the mask is flipped horizontally, the coils will line up perfectly, allowing for two wafers to be bonded easily. The coils are 2.92 mm by 5.92 mm, leaving a 40 µm gap at all sides from the edge of the etched wells. This is to ensure the coils fit entirely inside the wells. Figure 24 shows the coil mask. The process was designed so that only the coil mask needs to be changed to try other inductor designs, allowing for multiple iterations.

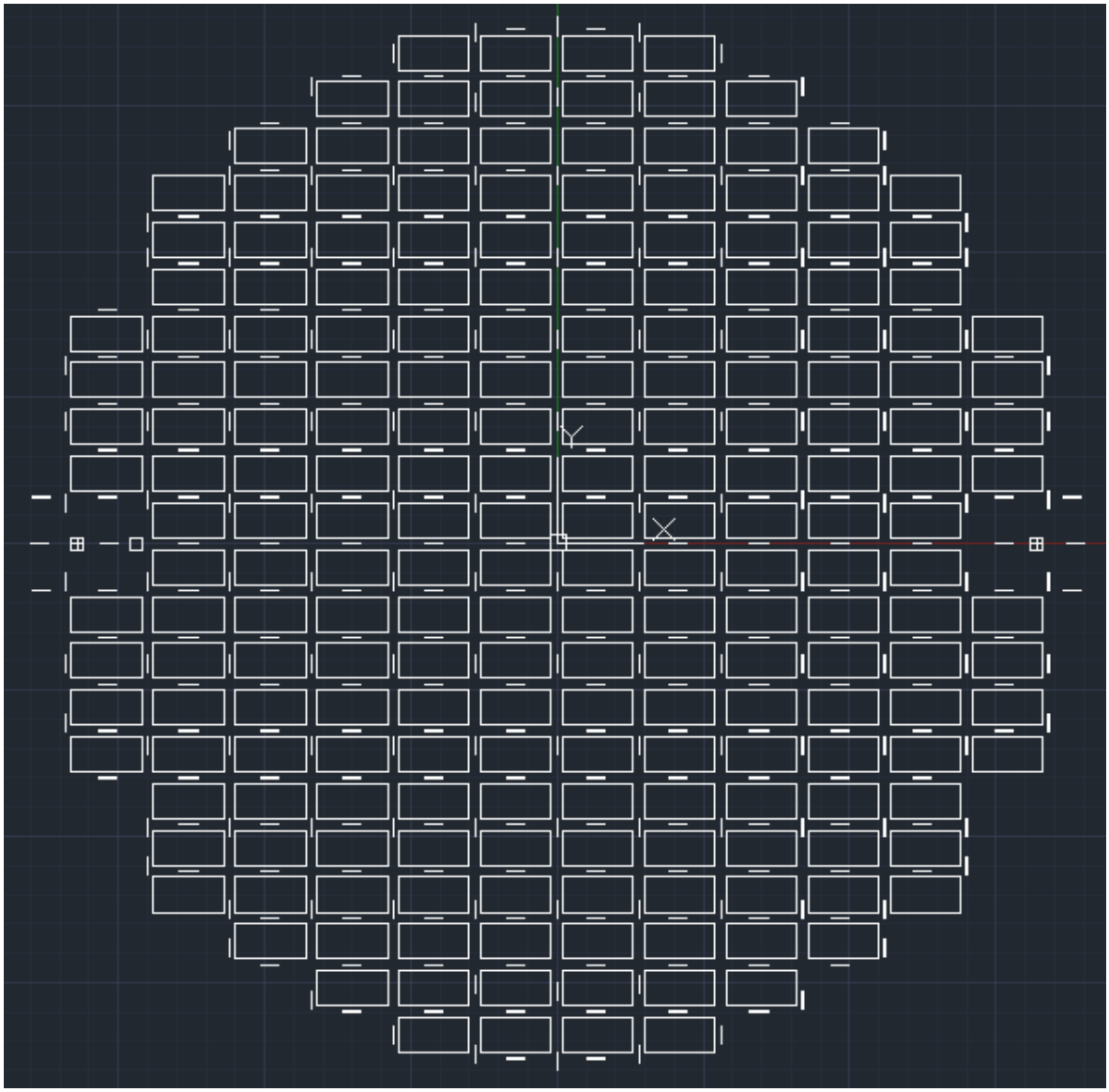

Figure 23. Etch mask for creating the sensor wells.

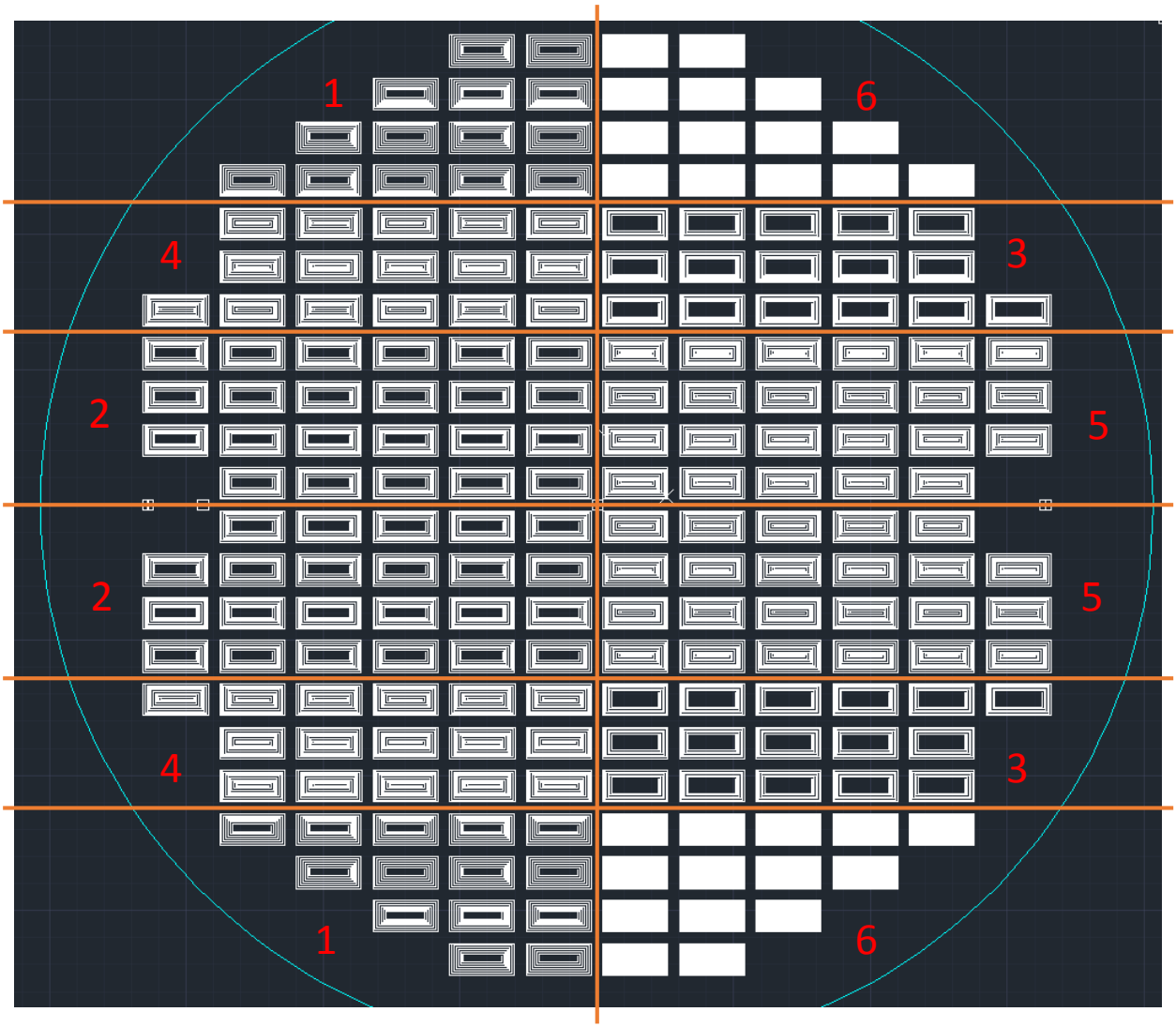

Figure 24. AutoCad mask with coil designs. The type of coil in each section is in red, with a horizontal line of symmetry.

Fabrication Procedure – Structural Sequence Summary

The entire fabrication process contains 10 main steps. Not only each step needs to be handled carefully and cautiously, fine tuning parameter values of every step have become the most challenging task to develop a working sensor prototype.

Step 1) Deposit nitride layer onto SOI wafer

Silicon nitride, Si_3N_4, is used here to create a "hard" mask as shown in Figure 25. Often in harsh processing conditions, for example wet chemical etches, photoresist is unable to withstand the

environment and thus adequately transfer the pattern into a physical structure on the wafer. In this case we are using a nitride hard mask to create the wells that form sensor cavities, as the processing occurs at a high temperature and pH.

Using photoresist to create pattern and subsequently etching the not covered Si_3N_4 areas to transfer the pattern into the nitride layer the hard mask is created for the next step. Photoresist is removed before proceeding to the next step, leaving just the patterned nitride layer in place.

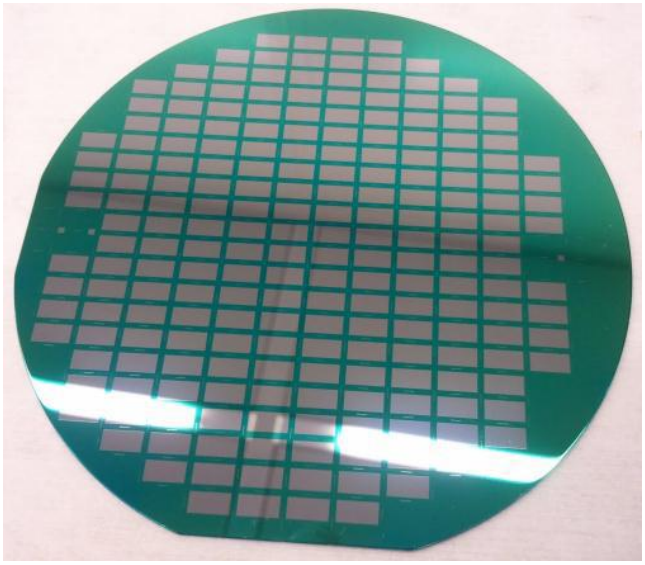

Figure 25. Si wafer with nitride hard mask

Step 2) Etch wells in the SOI wafer

Using a KOH bath, the silicon gets anisotropically (preferentially in the down direction) etched to create wells in the SOI device layer as shown in Figure 26. While it is also possible to etch Si using dry plasma methods, those tend to roughen the surface and make it unsuitable for metallization.

The KOH will etch along crystal planes as illustrated in Figure 27, this is the reason that we chose a <100> wafer. The angle between the bottom of the well and the side wall is 125.26°. Essentially, KOH preferentially attacks the <100> crystal plane, and etches the slowly exposed <111> plane at a much slower rate. Of course if a wafer were to be left in the solution long enough, eventually all of it would be etched away. There is a slight amount of undercutting (etching underneath the mask) that happens with

this process, so the final structure is slightly larger than the pattern (but negligibly so in our case). Subsequently, the hard mask is removed as it is no longer necessary for further steps (with this fabrication plan). Even though there is also a dry etching method to remove nitride, we use a wet etch method in phosphoric acid. This is to ensure no nitride remains anywhere on the wafer – in this case on the wafer edges, back side or between the wells. The deepest a silicon wafer could be etched is dependent on the width of the cavity due to the crystalline structure. The etching follows the crystal structure, causing it to go at an angle of 30°, instead of straight down. Therefore, the smaller the width, the shallower the etching can be. [24]

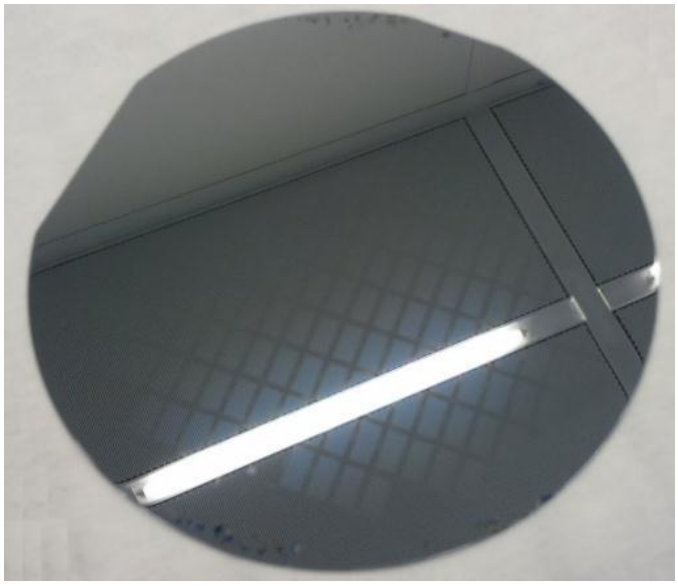

Figure 26. Si wafer with wells, reflecting ceiling

Step 3) Create 300 nm seed metal tracks in SOI and glass wafers

Again photoresist is used to create a pattern, this time covering all the areas that we do not want covered with metal. During the metal evaporation step that follows, the spaces between photoresist tracks get covered with metal, as well as the tops of the photoresist as shown in Figure 28. This photoresist can be removed later in the liftoff procedure as the photoresist is removed with acetone, taking the metal resting on top of it with it and leaving a pattern in the metal.

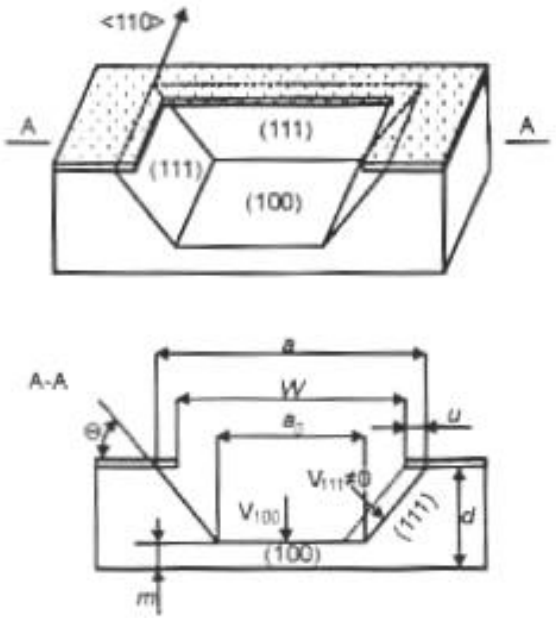

Figure 27. Geometric properties of a KOH Si etch

(From http://www.el-cat.com/silicon-properties.htm)

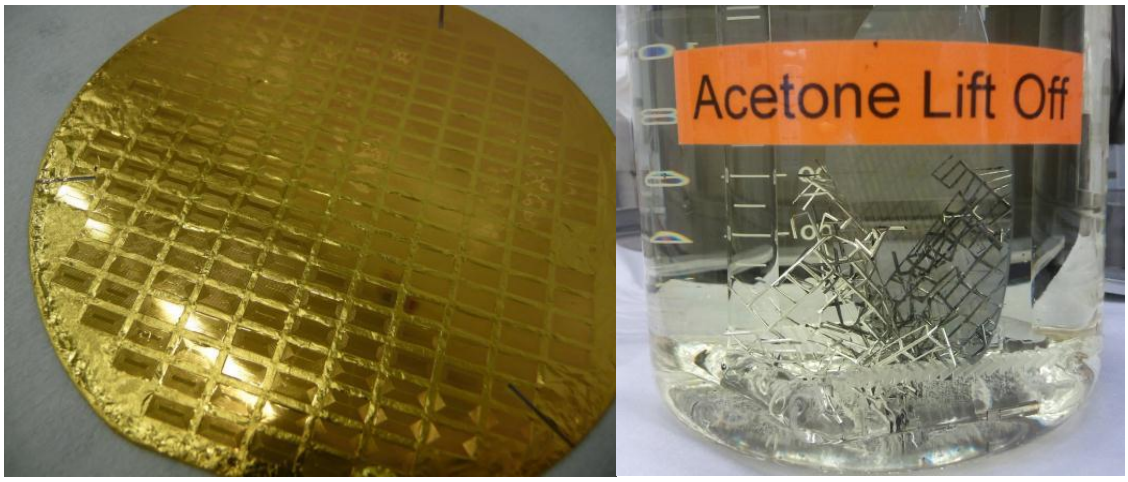

Figure 28 (A). Geometric properties of a KOH Si etch Glass wafer with evaporated Au pattern, previously used for testing but switched to Cu for process and cost reasons. **(B).** Wafer undergoing liftoff process with Ag test pattern

Step 4) Electroplating SOI and glass wafers to final metal thickness

To increase metal thickness to the final 8 µm, electrodeposition is performed using a power supply, and the wafer cathode plus copper sheet anode are immersed in the plating solution for previous electroplating equipment as shown in Figure 29(A). A holder is used in current electroplating equipment as shown in Figure 29(B). This is performed outside of the clean room, as the materials used are not

allowed inside due to contamination concerns, so care must be taken to not introduce extra particles onto the wafers during transport and plating.

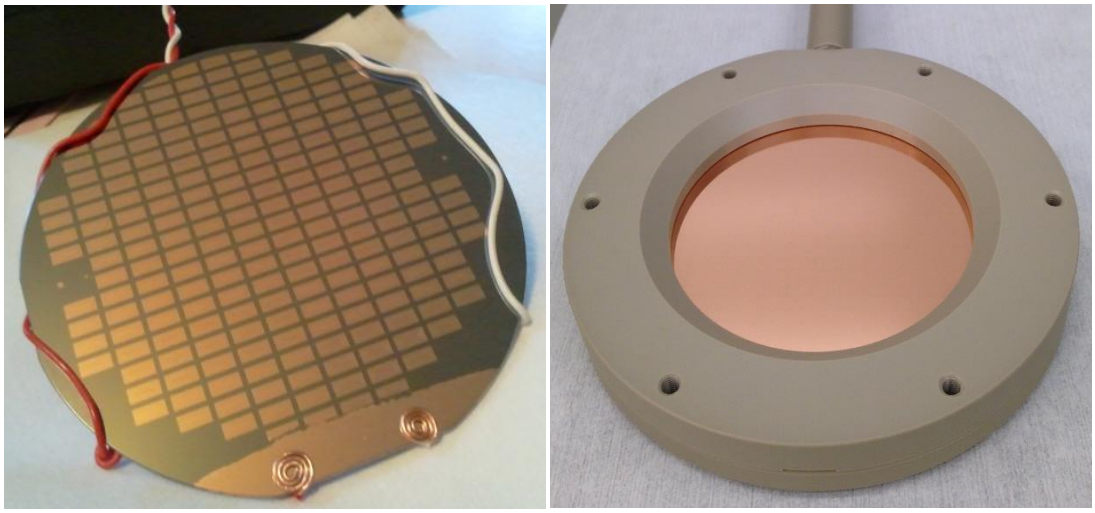

Figure 29 (A) Si wafer set up for Cu electroplating of previous equipment **(B)** Si wafer set up for Cu electroplating with holder for current equipment

Comparison of previous and current electroplating equipment

The electroplating process of previous equipment deposits copper uniformly everywhere onto the wafer, even the back. Additionally, since the plating solution is corrosive to the currently used photoresist, it dissolves before the final thickness is achieved. The current electroplating equipment with well controlled AC power source deposits copper uniformly. The current electroplating holder could realize circular electroplating touching and protect the backside of wafer away from electroplated copper. The quality of electroplating has significantly improved because of new electroplating equipment. Even though, the quality of electroplating is affected by many factors, such as stress of materials, uniformity of plating layer, temperature, current control and timing which need to be carefully adjusted.

The etching process after electroplating needs to be in one go – etching, washing and checking seems to result in patchy effects on the wafer. This is what has happened to our first 33 µm wafer, the yield is now low because of the etch rates are wildly different across the wafer. Warping happens with 20 and

40 µm plated wafers, especially before any patterning. Once the well pattern has been etched, this warping significantly decreases but still remains – there is a question of whether this film stress of Cu may alter our pressure membrane properties. Looking at etch times it has also been over-etched, yet there are areas that are not yet etched. Electroplating process and etching process seems very repeatable and established as shown in Table 8 and Figure 30.

Table 8. Cu etch table:

Trial #	Thickness (µm)	Etch time (min)	Plating time (h)	Plating Current (A · min)
1 (flat)	5	2	0.51	15
2 (flat)	18.27	9	1.25	60
3 (flat)	33.17	32	2.66	120
4 (SiO_2 wells, top)	39	26	2.66	120
5 (Si wells, bottom)	40	26	2.66	120
6 (SiO2)	15	8	1.25	60
7 (Nitride)	19	9	1.25	60
8 (Si old)	19	9	1.25	60

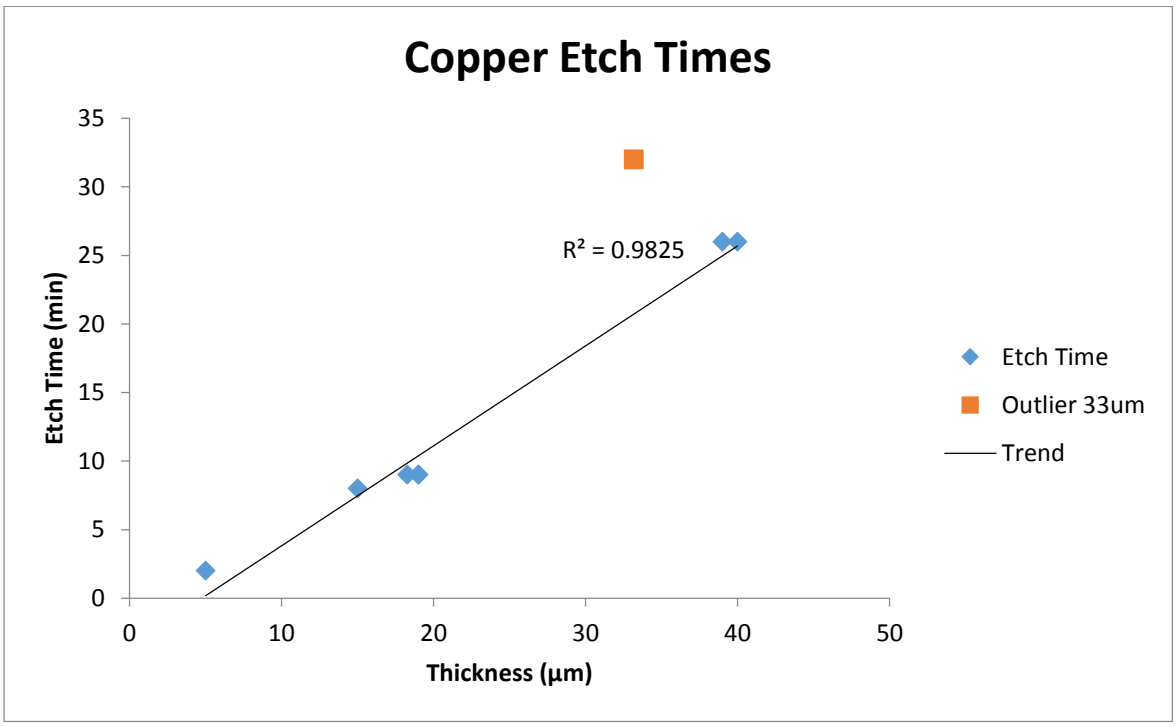

Figure 30 Electroplated copper thickness vs Copper etch times

Step 5) Etching metal layer to trim to final shape on both SOI and glass wafer

It is difficult to realize a perfect uniform surface during the electroplating process because so many characters need to be handled well simultaneously as mentioned before. However, a pattern does persist in the metal: where seed layer was previously deposited, there is good adhesion, elsewhere the adhesion is poor.

While this difference is enough to remove large pieces of excess metal (for example from the back of previous equipment, or between the wells), it is not enough to remove excess metal from between the coil tracks, as that space is only 20 µm wide as shown in Figure 31. Another photoresist layer is applied and aligned to the pattern to protect the present coil tracks from etch, ensuring that the excess metal is preferentially removed.

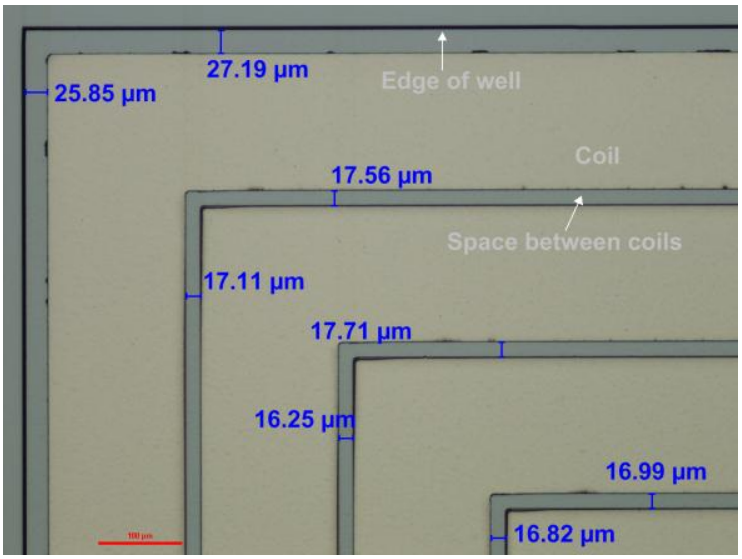

Figure 31 Measurements performed on final metal tracks developed on a metalized Si wafer using a microscope camera system

Step 6) Yield calculation on SOI and glass wafer

Under a microscope, a map of continuous coils without shorts between the tracks must be noted for both the SOI and glass wafers. This is important to later distinguish sensors that are electrically sound from those that will never yield a functioning sensor due to voids in the tracks or shorts between them. Once the two wafers are bonded there is no way to tell other than by measuring resonant frequency, at

which point an element of uncertainty is added as to why the sensor failed – due to processing before bonding, or processing after bonding, or due to receiver mistakes. Troubleshooting can be more difficult if this step is skipped. Figure 32 shows one whole test sensor field microscope image with dicing marks around it.

Step 7) Anodic bonding

Using heat and voltage, the glass and SOI wafers are bonded together under vacuum to create a single piece with sensor cavities. Any interfering particles can also cause voids, but do not prevent the rest of the wafer from bonding, as shown in Figure 33.

The process of anodic bonding, to bond the two wafers together, requires about 0.5 mm of flat area on all sides for contact [24]. This means the wafer will have to be larger than the metal coils on all sides.

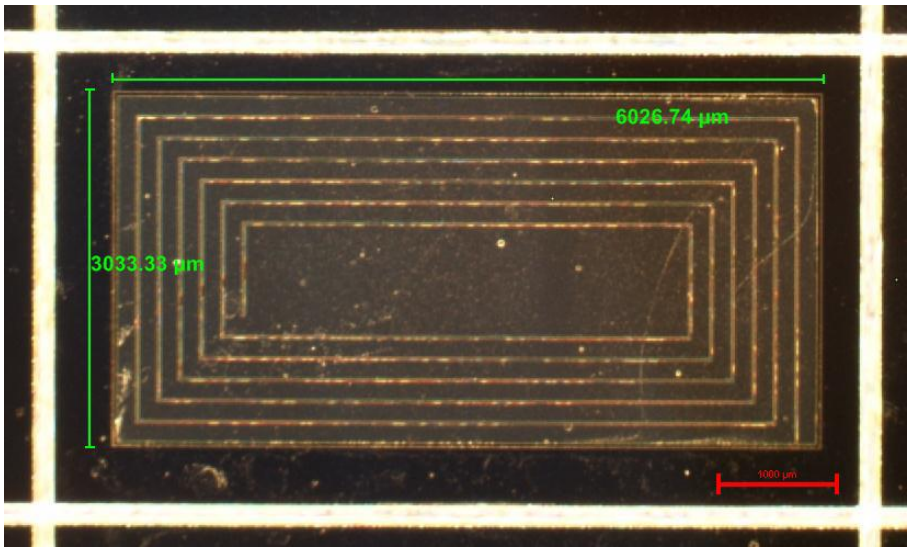

Figure 32 One whole test sensor field microscope image with dicing marks around it

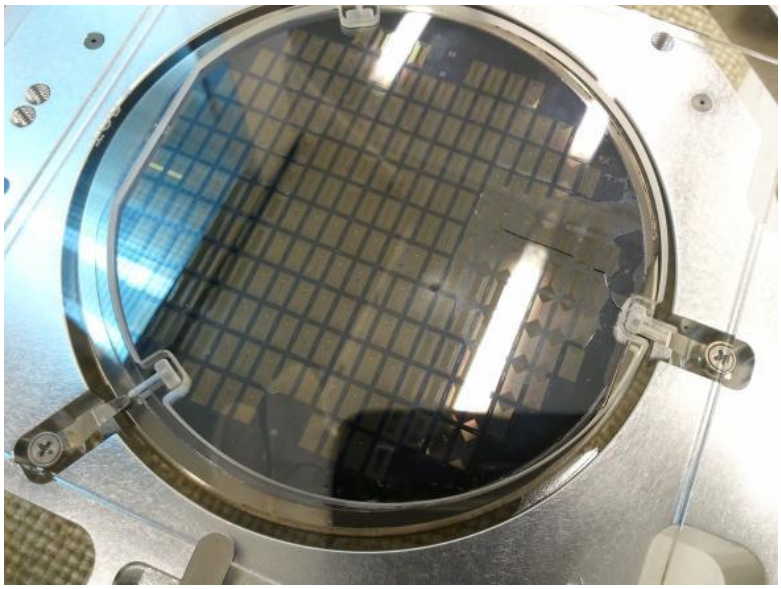

Figure 33 Anodically bonded glass and SOI wafers on chuck for aligned bonding, with flags retracted. Bottom right flag failed to retract, creating a crack and large void. Wafer could still be diced away from the affected area though

Step 8) Handle removal

Now the SOI handle layer is removed using a dry etch method to selectively away etch the handle as shown in Figure 34, and no other Si surfaces. The glass wafer now serves as the handle.

Also, since the SiO_2 insulating layer is often under considerable stress, that layer must also be removed for the sensor to mechanically function properly, this is most conveniently done using a wet etch

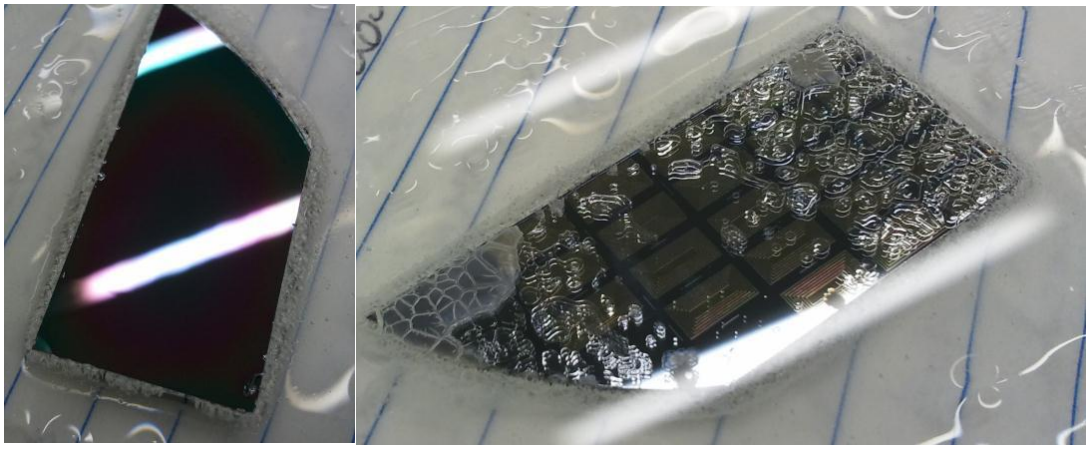

Figure 34 SOI bonded to glass, piece of whole wafer mounted using clear crystalbond mounting method on a fused silicate wafer, with the handle removed. **(A)**. Si device layer **(B).** Glass layer, bubbles are from crystalbond heating during the etch

method because dry etching SiO_2 usually leaves residue and is much slower. The glass is not attacked during this procedure at a significant enough rate, as its chemical composition is slightly different from pure SiO_2. There should be a subtle color change to plain gray once all the SiO_2 is gone.

Step 9) Dicing

The final sensors are obtained by sawing the wafer stack into corresponding pieces. Currently each sensor is 7 mm × 4 mm in size. This step also dictates that the final shape of the sensor must be rectangular. Dicing saw inside of the WCAM is used to cut the whole 4 inch wafer into multiple small pieces as shown in Figure 35. Outside of the WCAM facilities there are laser cutting instruments that could create any shape sensors, if so desired. However, this takes more time and costs more. The implantation holder (plug) that the sensor is embedded into currently compensates for these sharp features that would provoke an unfavorable reaction from the body as shown in Figure 36.

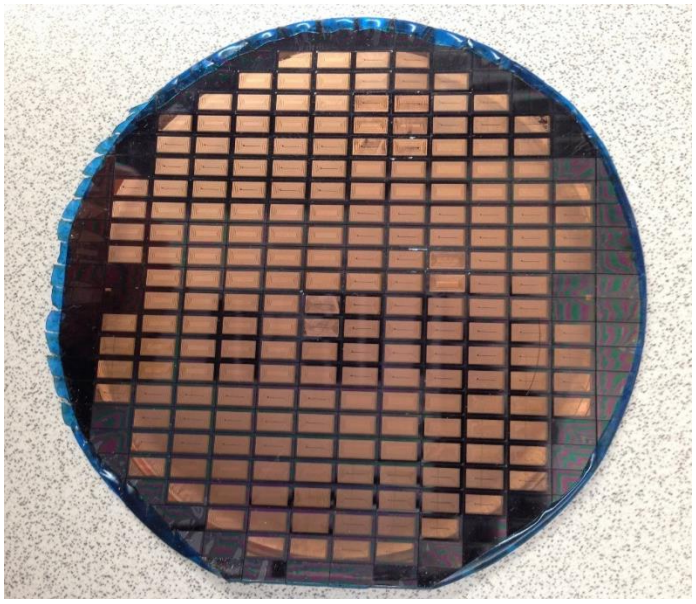

Figure 35 Diced multiple sensors of silicon layer used dicing saw tool

Figure 36 Single sensor sawed out and inserted into plug.

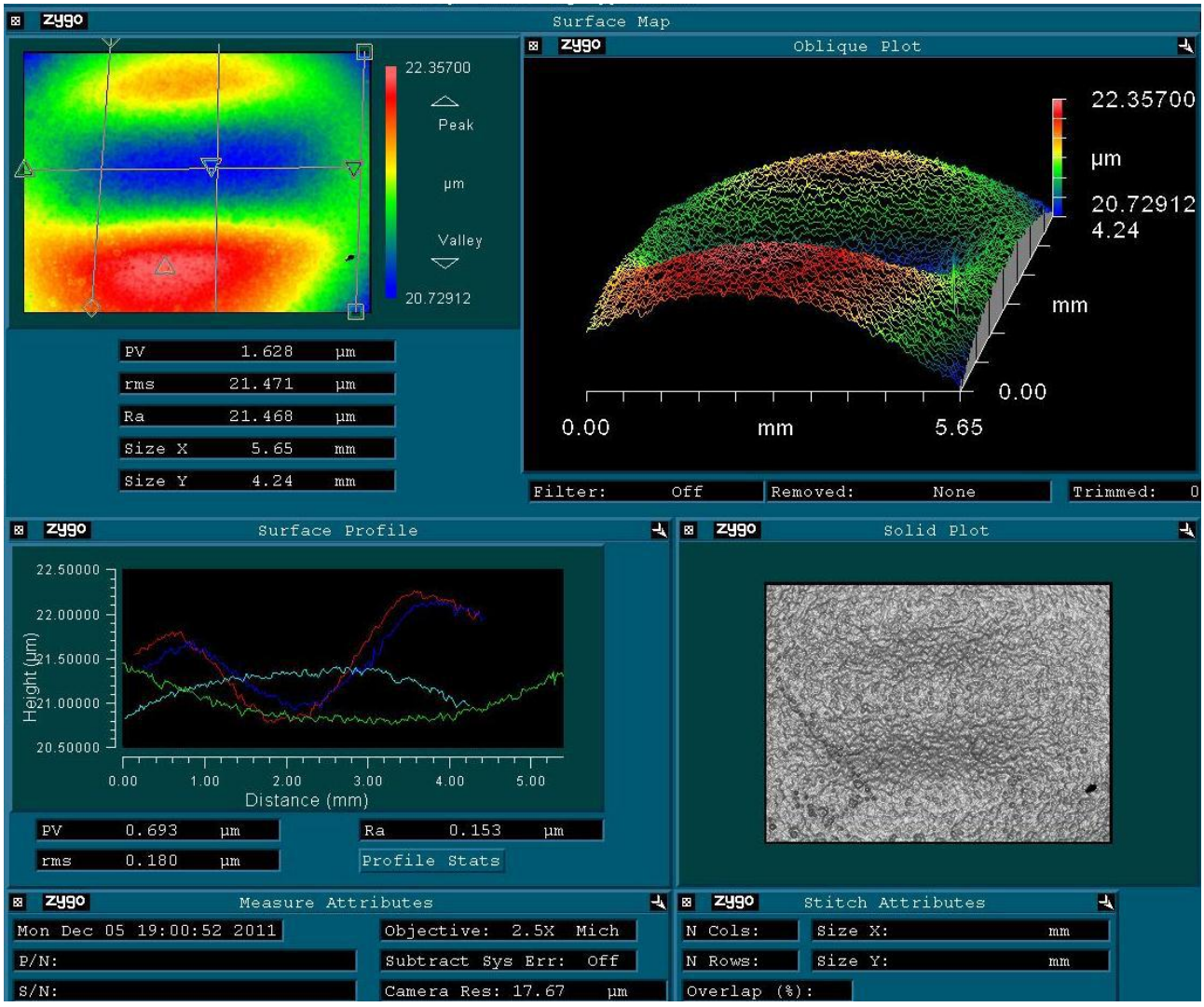

Figure 37 Single well interferometry membrane deflection result. Top left is a 2D depth plot relative to a calibration point on the edge of the wafer. Oblique plot is a 3D representation of that same result. Surface profile shows the height distribution along the lines drawn on the top left plot: red and dark blue are vertically across deflected sensor membrane, light blue is vertically across the edge of the membrane, light green is the horizontal line. The Solid Plot window is a camera image.

Step 10) Verification

Sensor integrity can be ascertained by observing the bowing of the Si membrane, which can be seen unaided by instrumentation – if there is no deflection, the vacuum within has failed. To precisely determine the amount of deflection of the membrane the smooth Si membrane surface can be scanned by the Zygo interferometer as shown in Figure 37 at the Materials Science Center (MSC).

Electrical verification of the final sensors can be made by either placing them on the reader, or by using the spectrum analyzer to find a resonant peak as shown in Figure 38.

Sensor Testing

The first iteration without electroplating process of coil designs was successfully made in the clean room, allowing for sensor testing. The sensors were placed on a spectrum analyzer, which is able to excite the coils with any frequency range needed. However, no resonant peak could be detected for measurement. Examining the coils did not reveal any shorts across the coils tracks, leading us to believe the resistance of the coils was too high. Also, the coils were not able to be connected together, resulting in a system inductance that is half of the inductance of a single coil since the coils are in parallel. Both the high resistance and low inductance lead to a lower quality factor making it much more difficult to detect the resonant frequency. Figure 38 shows the resonant frequency detecting difference with different quality factors. It is easy to find out which value is the resonant frequency with a high quality factor in Figure (38A). However, it is really difficult to find out the resonant frequency value with a low quality factor in Figure (38B).

To understand quality factor better, an experiment was designed to see the effect of quality factor on resonant peak detection. It was determined that the resonant peak of a coil with a quality factor of below 6 is very difficult to detect. Therefore, it is crucial to raise the quality factor in the coil design.

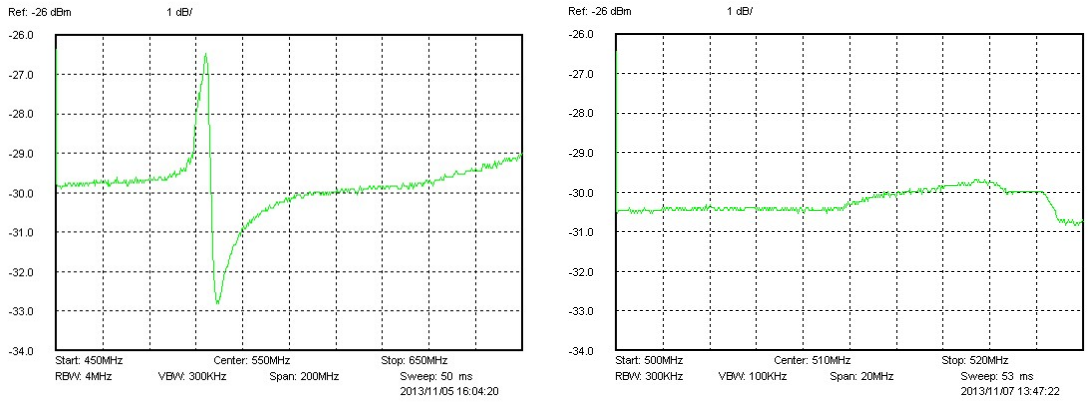

Figure 38 (**A**). Resonant frequency detecting with high quality factor by spectrum analyzer (**B**). Resonant frequency detecting with low quality factor by spectrum analyzer

To test the accuracy of the calculations, CST Microwave Studio was used to find the resonant frequency of coil 4. The two coils were set up 3 µm apart and not connected, as shown in Figure 39.

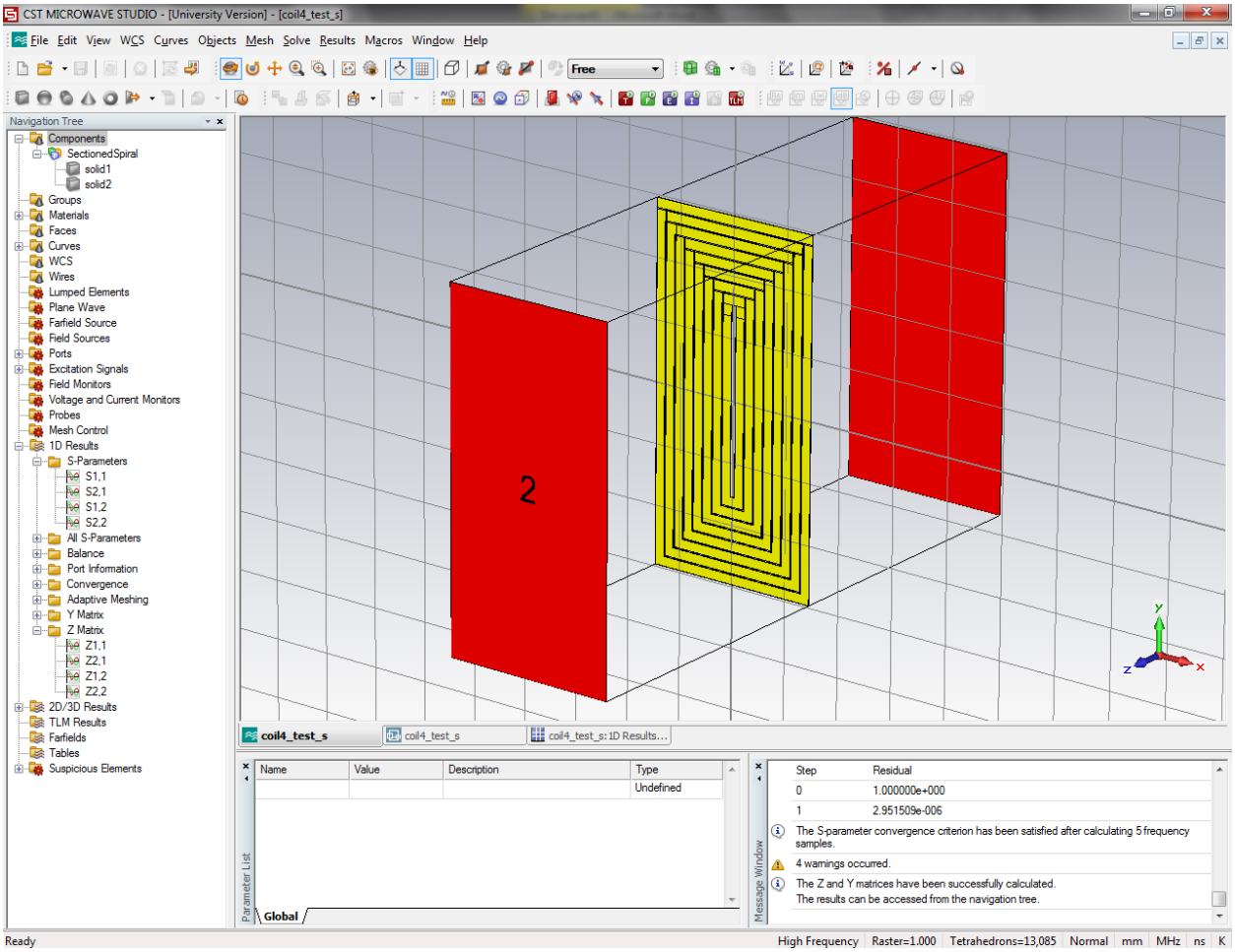

Figure 39. CST Microwave Studio set up for coil 4.

According to Table 7A, this should give a resonant frequency of about 81 MHz. After simulating the sensor, a resonant frequency of 91 MHz was found. This means the Matlab calculations overestimate the inductance by about 10 %. The error is expected, because the Matlab calculations do not take into account losses between turns and are therefore best case simulations.

Realizing a high sensor sensitively to the ICP changing is a major goal in sensor fabrication. The frequency of a resonant tank circuit with a high quality factor varies sensitively with ICP changing. To achieve high quality factor, the metal coils must be sufficiently thick in the range of 10 µm. The maximum thickness that may be produced using evaporation technology in a cleanroom is only 2 µm. Metal coils so fabricated have higher resistance and lower quality factor which is not usable. Electroplating outside the cleanroom is the best option to achieve thickness greater than 10 µm. Table 9 summarizes the predicted electrical properties, resonant frequency and quality factor after measuring resistance, inductance value and calculating capacitance value according to different distance between two coil layers. The inductance value is 0.00028 mH and the resistance value is 2.47 Ω. According to the value of Table 9, the decreased value of resistance significantly improves the value of quality factor. With the high quality factor, the spectrum analyzer machine could be used to test the resonant frequency. The resonant frequency of first successful working functional coil detected by the spectrum analyzer machine is shown in Figure 40.

Table 9. Table summarizing the electrical characteristics of different distance for a specific coil with inductance value is 0.00028 mH and the resistance value is 2.47 Ω

Predicted Distance (µm)	Capacitance (pF)	Resonant Frequency (MHz)	Quality Factor
5	31.86	53.29	37.95
10	15.93	75.36	53.68
15	10.62	92.30	65.74
20	7.97	106.54	75.88
25	6.38	119.08	84.81
30	5.31	130.53	92.97

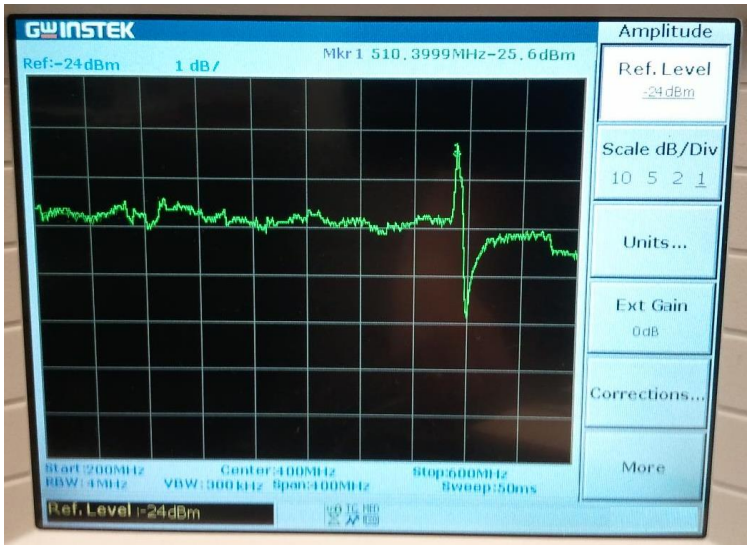

Figure 40. First working functional coils with electroplating process detected by spectrum analyzer

Methods to improve the Quality factor:

Besides of the electroplating method, two other methods were tried to improve the quality factor. The first method was comparing whether isolation processes before electroplating could improve the quality factor. The second method was checking the effect on quality factor of addition of a metal wound coil.

Isolation method

All three types of wafers have been electroplated to approximately 20 µm thickness: bare Si, Si-SiO2, and Si-Nitride-SiO2-Nitride. They have been pre-processed with photoresist and are standing by for the MA6 aligner to be working again. A layer of SiO_2 has been successfully sputtered onto pieces of Cu coils without inducing oxidation: this is promising as we can now deposit a dielectric on top of the coils to increase the capacitance and mutual inductance.

All 3 types of wafers have been patterned to their coil shape very successfully and Cr etch which takes more than 4 h each. The addition of oxide added some harmonics, does not change the primary peak frequency. Figure 41 shows the resonant frequency detecting by spectrum analyzer for three types of whole wafers and no Cr etch yet, 5 dB/div.

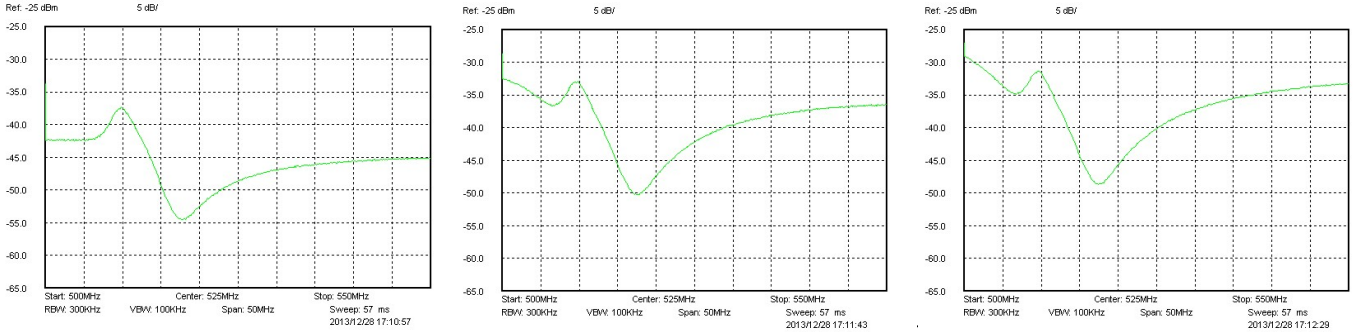

wafer **(C)** Nitride-oxide sandwich wafer

(A) Si coil by itself

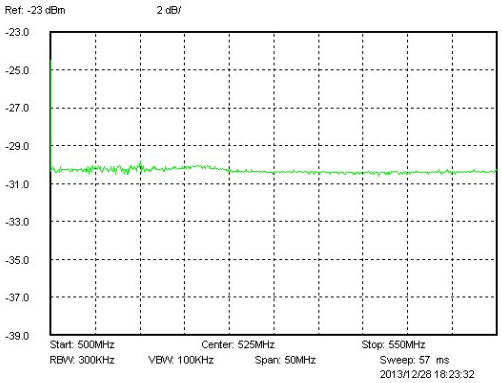

(B) Wound coil by itself

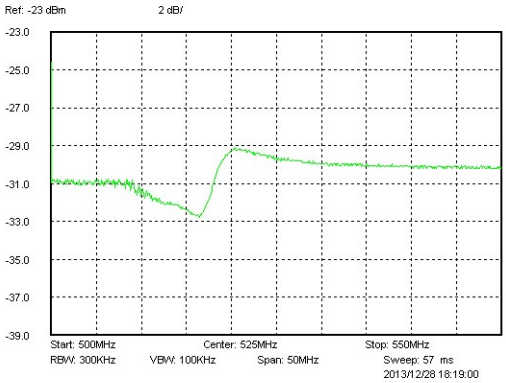

(C) 2 coils, turns in the same direction

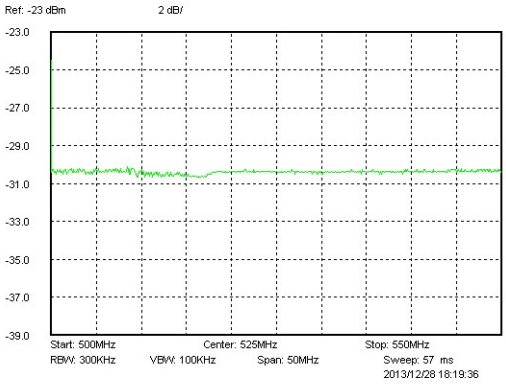

(D) 2 coils, turns in opposing directions

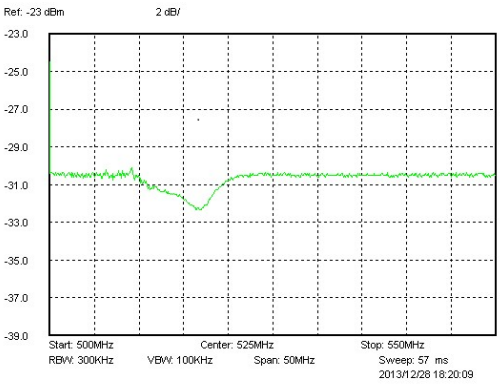

Figure 42. The resonant frequency detection of spectrum analyzer machine result of **(A)** Si coil, **(B)** wound coil, **(C)** two coils in same direction and **(D)** two coils in opposing direction separately as 2 dB/ div.

Addition of metal wound coil method

Addition of metal wound coils to the back of a sensor did increase the *Q* factor, it remains to be seen whether it overlays the signal or helps it (with a functional moving sensor). Figure 42 shows the resonant frequency detection result of Si coil, wound coil, two coils in same direction and two coils in opposing direction separately as 2 dB/div. The back coil results show that the frequency of the wound coil is slightly different as it dominates. The coils have to be wound in the same direction to improve quality factor. It does not change the frequency of the combination, but rather adds harmonics. Trying to match the frequencies exactly might be challenging for future testing. Figure 43 shows the resonant frequency detection result of Oxide coil, two oxide coils in the same direction and two oxide coils in opposing directions separately as 1 dB/div. With the SiO_2 covered coils that have the same frequency, when put together amplification of varying degrees (depending on the distance between the coils and the material) has been observed when the coils are wound in a continuous (same) direction, but a canceling effect when they are wound in opposing directions as expected.

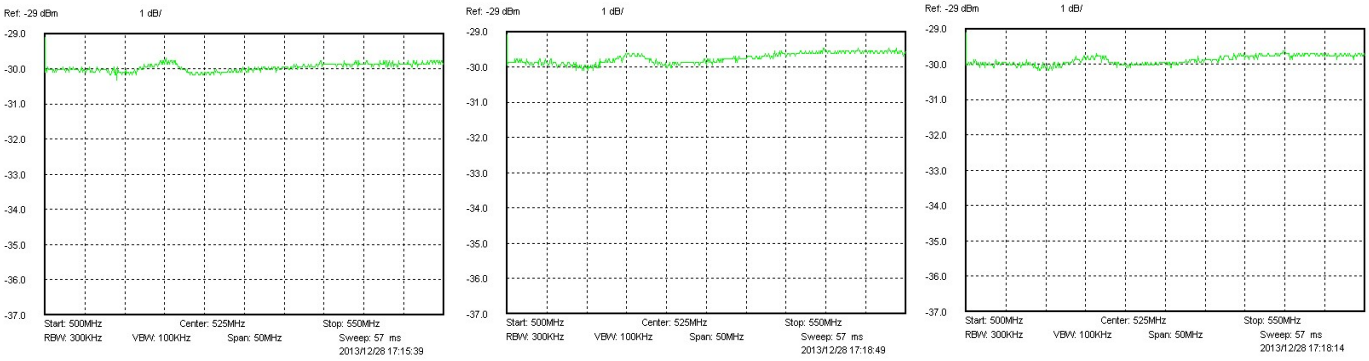

Figure 43. The resonant frequency detection of spectrum analyzer machine result of **(A)** single Oxide coil, **(B)** two oxide coils in the same direction, **(C)** two oxide coils in opposing direction separately as 1 db/ div.

Electroplating existing issues

Figure 44 shows the three different existing issues during the electroplating silicon wafer layer process. The seed layer is the silicon wafer, the adhesion layer is the Cr layer itself or Cr and Cu combination layer.

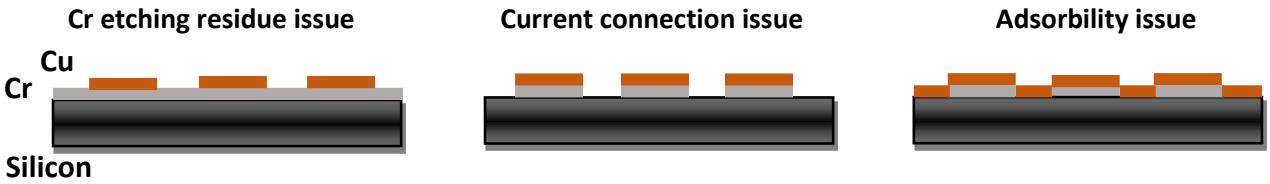

Figure 44. Three different existing issues during the electroplating silicon wafer layer process. **(A)** Cr etching residue issue **(B)** Current connection issue **(C)** adsorbility issue

Figure (44C) shows the adsorbility issue. The majority reason that Evaporated Cr + Lift off + Evaporated Cr + Electroplating Cu failed before is the adhesion layer evaporated Cr and evaporated Cu should be in the same vacuum evaporation round. Once the Cr touches the atmosphere during the lift off step, it loses the adhesion layer function. If the lift off step is not included in the whole process, the Cr etching should be handled well. Figure (44A) shows the Cr etching residue issue. The Cr dry etching recipe/technology in WCAM now has a residue issue. The Cr dry etching residue issue exists for a period of time and no good method can resolve it so far. Also the whole wafer should have metal to let the current go through each coil when electroplating. Otherwise, it causes the current connection issue as shown in Figure (44B). That is the reason lift off cannot be done after evaporating Cr and Cu in the same vacuum evaporation round. The next step is to combine Evaporated Cr + Lift off + Evaporated Cr + Electroplating Cr and RTA, whether the result can solve the whole absorbability or not is about to be confirmed and tested.

The RTA (rapid thermal annealed) experiment is on the way. RTA technology is a good method to increase Cr adsorbability after electroplating to optimize reasonable yield of uniform Cu layer. After RTA at 400 °C for 30 s, the resistivity of Cu deposits was reduced. Moreover, after annealing, the intensity of electroplated Cu increases and Cu become more smooth since small grain structure disappears.

If the above method fails, then the next step is to research and find out a method of Cr wet etching instead of Cr dry etching. Hopefully the metal selectivity performs better in wet etching, just etching Cr and not affecting the Cu area.

Implant holder

Given the dimensions and surgery specifications, a plastic holder for the sensor has been developed by graduate student Gerhard van Baalen. The holder keeps the sensor in place and exposes the diaphragm to the intracranial pressure. The design of the holder matches the attachment method for the Codman pressure sensor. The material of the holder was chosen to be plastic (non-metallic) in order to avoid complications of signal shielding from the sensor to the oscillator. The plastic also needs to be biocompatible for long periods of implantation in order to avoid scar tissue build up. Of concern is the biocompatibility of the exposed silicon diaphragm, because if tissue builds up on the sensor, the sensor will cease working. Therefore, the holder should be as biocompatible as possible, to avoid any additional biocompatibility issues.

The design of the holder is a large cap to be secured to the top of the skull, with a long stem to get into the brain. At the end of the stem is a pocket that is 4 mm x 7 mm to hold the sensor. The silicon diaphragm is exposed, but the rest of the sensor is within the pocket. The holder was made as round and smooth as possible to increase biocompatibility, and the cap was slightly curved to match the curvature of the skull. In the cap, there is a wide slot that allows a catheter of about 3 mm diameter to be inserted through the same hole as the holder. Also are two screw holes for the standard surgery screws to secure the holder to the skull. The width of the pocket is 5 mm to be inserted through the 5 mm slit in the Dura, and the length of the stem should be altered per patient.

The material of the holder has been decided to be UHMWPE or Watershed XC 11122. UHMWPE has been used in many implants before, specifically hip replacements, and has been proven to be

biocompatible [25]. However, UHMWPE has to be machined or molded into the shape needed for the holder. Watershed XC 11122 is a USP Class VI biocompatible material, and is a resin for rapid prototyping. Specifically, Watershed XC 11122 can be used with stereo lithography to create a biocompatible prototype quickly [26].

This holder can be attached to the skull and then covered with skin, making the sensor fully implanted without a pathway to the external environment. The implantation can be permanent since materials of the sensor and the holder do not degrade in the body. Figure 45 shows the design and dimensions of the implant.

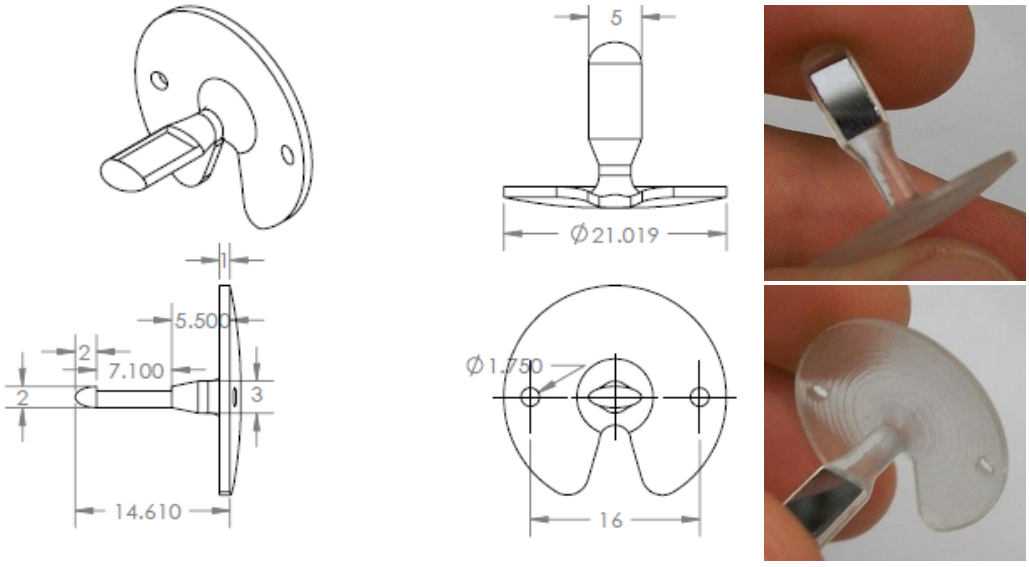

Figure 45. Dimensions of plastic implant.

Conclusion and Future work

In terms of sensor function, it is very clear that resistance is currently the major obstacle to proper sensor function. While electroplating can help mitigate that problem, the geometric sensor design [27] can be optimized to achieve an even higher *Q*. Since our current sensor geometry does not reflect these ideas, does not work the best with the anodic bonding alignment tool, and could use improvement in terms of alignment mark design, it makes sense to incorporate these ideas into the next generation masks.

The current sensor fabrication approach is a combination of the electroplating approach coupled with wet etching. The poor adhesion between bare Si and Cu can be exploited to expedite etching where Cu needs to be removed, and the photoresist applied to tracks that need to remain helps protect them from the etch solution. In the future, this method will likely give way to an appropriate photoresist mold.

The remaining research work will focus on refining the design of the coil to improve the *Q* factor that may be realized subject to the limitation of available MEM fabrication technology. Increasing electroplating yield, reliability and uniform is current biggest difficulty. Also, more simulation and experiments will be performed to determine optimal number of turns and thickness of metal coils. After making the working functional sensor, then the next step is combining working coils into a functional sensor for pressure testing and calibration. The next step is scaling up the reader frequency to match the working sensor. The last step is performing in vitro and in situ testing of the sensor prototypes and evaluating their performance.

Reference:

[1] Hydrocephalus Association <http://www.hydroassoc.org/>

[2] Smith M. Monitoring intracranial pressure in traumatic brain injury. Anesth Analg 2008; 106: 240−248.

[3] Mokri B. The Monroe-Kellie hypothesis: Application to CSF volume depletion. Neurology 2001; 56(12): 1746−1748.

[4] Brian North, Noninvasive Monitoring of Intracranial Pressure, Recent Patents on Biomedical Engineering 2009, 2, 209−216.

[5] Mayhall CG, Archer NH, Lamb VA, Spadora AC, Baggett JW, Ward JD, Narayan RK Ventriculostomy-related infections. A prospective epidemiologic study. N Engl J Med. 1984 Mar 1; 310(9):553−9.

[6] Holloway KL, Barnes T, Choi S, Bullock R, Marshall LF, Eisenberg HM, Jane JA, Ward JD, Young HF, Marmarou A Ventriculostomy infections: the effect of monitoring duration and catheter exchange in 584 patients. J Neurosurg. 1996 Sep; 85(3):419−24.

[7] Zabramski JM1, Whiting D, Darouiche RO, Horner TG, Olson J, Robertson C, Hamilton AJ. Efficacy of antimicrobial-impregnated external ventricular drain catheters: a prospective, randomized, controlled trial. J Neurosurg. 2003;98(4):725−730.

[8] Zhong J, Dujovny M, Park HK, et al. Advances in ICP monitoring techniques. Neurol Res 2003; 25: 339−350.

[9] Miyake H, Ohta T, Kajimoto Y, Matsukawa M. A new venticuloperitoneal shunt with a telemetric intracranial pressure sensor: Clinical experience with 94 patients with hydrocephalus. Neurosurgery 1997; 40(5): 931−935.

[10] Stefan Welschehold, MD, MA Eva Schmalhausen, et al. First Clinical Results With a New Telemetric Intracranial Pressure-Monitoring System. Neurosurgery 70:ons44 (2011)

[11] Djordje Popovic, Michael Khoo1 and Stefan Lee, Noninvasive Monitoring of Intracranial Pressure, Biomedical Engineering 2009, 2, 165−179.

[12] Alperin, N.: Method of measuring intracranial pressure. US patent 5993398 (1999).

[13] The Brain Trauma Foundation. The American association of neurological surgeons. The joint section on neurotrauma and critical care. Indications for intracranial pressure monitoring. J Neurotrauma 2007; 24: S37−44.

[14] Wagner N, Walsted A. Postural induced changes in intracranial pressure evaluated non-invasively using the MMS-10 tympanic displacement analyzer in healthy volunteers. Acta Otolaryngol Suppl 2000; 543: 44−47.

[15] Dr. Joshua Medow. “Doctor’s Basement tinkering Leads to Development of Intracranial Pressure Monitor.” School of Medicine and Public Health. (October 25, 2011). <http://www.med.wisc.edu/news-events/joshua-medow-basement-tinkering-leads-to-intracranial- pressure-monitor/32282>

[16] LC circuit introduction <http://en.wikipedia.org/wiki/LC_circuit>

[17] Quality factor <https://en.wikipedia.org/wiki/Quality_factor>

[18] Matthew A. Hopcroft, William D. Nix, Thomas W. Kenny. “What is the Young’s Modulus of Silicon?” JOURNAL OF MICROELECTROMECHANICAL SYSTEMS, VOL. 19, NO. 2, pp. 229 – 38. (APRIL 2010).

[19] S. Timoshenko. “The Theory of Plates and Shells.” McGraw-Hill, pp. 180 – 228. (1959).

[20] Carter C. Collins. “Miniature Passive Pressure Transensor for Implanting in the Eye.” IEEE Transactions of Biomedical Engineering. Vol. 14, No. 2, pp. 74-83. (April 1967).

[21] Youbok Lee. “Antenna Circuit Design for RFID Applications.” Microchip Technology Inc. pp 1 – 50. (2003).

[22] Irving M. Gottlieb. “Practical Oscillator Handbook.” Newnes, Oxford. (1997).

[23] J. Coosemans, M. Catrysse, R. Puers. “A readout circuit for an intra-ocular pressure sensor” *Sensors and Actuators A.* Vol. 110, pp. 432–438. (2004).

[24] Efremov M, Dry etching of copper using chlorine, Russian Microelectronics, 2002, Mikroelectronika 31(3), p.179-192

[25] S.M. Kurtz. “UHMWPE Biomaterials Handbook.” Elsevier Academic Press. UHMWPE Lexicon. (2012). <http://uhmwpe.org>

[26] “WaterShed XC 11122.” DSM Somos. (2009). http://www.dsmsomos.com

[27] H. J. De Los Santos, On the Ultimate Limits of IC Inductors – An RF MEMS Perspective, 2002, Electronic Components and Technology Conference Proceedings, 52, p. 1027 – 1031